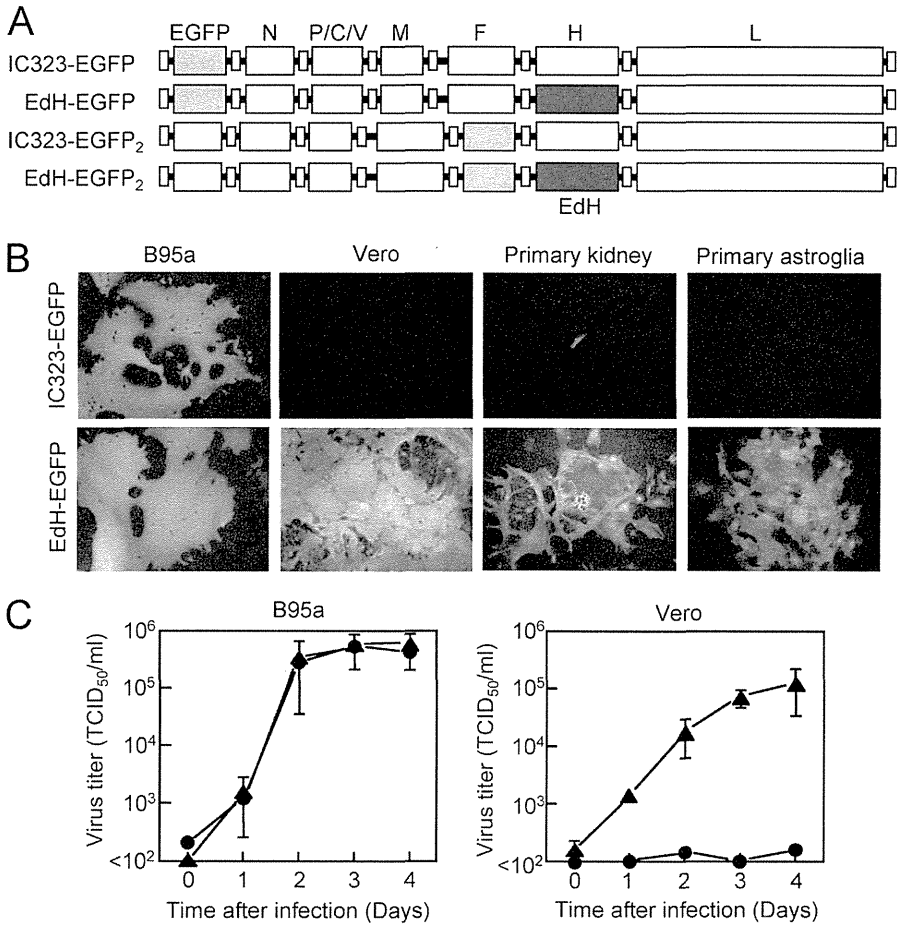

FIG 1 Generation, dissemination, and growth of recombinant measles virus (MV) having the hemagglutinin (H) protein of the Edmonston vaccine strain. (A) Schematic diagram of the genomic organizations of IC323-EGFP, EdH-EGFP, IC323-EGFP$_2$, and EdH-EGFP$_2$. (B) B95a, Vero, primary cynomolgus monkey kidney, and primary cynomolgus monkey astroglial, cells were infected with IC323-EGFP or EdH-EGFP. The MV-infected cells were visualized with EGFP autofluorescence at day 2 (B95a), day 3 (Vero), day 4 (primary kidney), or day 3 (primary astroglia). (C) Replication kinetics of IC323-EGFP$_2$ and EdH-EGFP$_2$. B95a cells and Vero cells were infected with IC323-EGFP$_2$ (circles) or EdH-EGFP$_2$ (triangles) at a multiplicity of infection (MOI) of 0.01 tissue culture infective dose (TCID$_{50}$)/cell. Cells and media were harvested at days 0, 1, 2, 3, and 4, and infectivity titers were assessed as TCID$_{50}$ using B95a cells.

follows; interleukin-12/23 (IL-12/23) (p40), 1.11 pg/ml; gamma interferon (IFN-γ), 0.30 pg/ml; IL-2, 0.73 pg/ml; IL-4, 1.25 pg/ml; IL-5, 0.26 pg/ml; IL-17, 0.13 pg/ml; IL-6, 0.40 pg/ml; tumor necrosis factor alpha (TNF-α), 0.86 pg/ml; IL-1β, 0.16 pg/ml; and monocyte chemoattractant protein 1 (MCP-1), 0.91 pg/ml.

RESULTS

Generation of recombinant MV strains expressing EGFP. To compare the cell specificities *in vitro* of wild-type MV and wild-type MV bearing the H protein of the Edmonston vaccine strain, we generated EdH-EGFP from wild-type IC323-EGFP (12). IC323-EGFP and EdH-EGFP (Fig. 1A) have the EGFP gene preceding the N gene and induce a strong EGFP fluorescence in infected monolayer cells. For *in vivo* infection, we generated IC323-EGFP$_2$ and EdH-EGFP$_2$ (Fig. 1A), having the EGFP gene between the F and H genes, because a previous report using canine distemper virus (CDV) indicated that a CDV strain having the EGFP gene preceding the N gene had reduced overall CDV gene expression and was less virulent (38). IC323-EGFP$_2$ and EdH-EGFP$_2$ induced very weak EGFP fluorescence in infected monolayer cells (data not shown) because of the polar effect of paramyxovirus transcription (17).

Infection of primary cell culture with recombinant MV strains. We first examined the cell specificities of IC323-EGFP and EdH-EGFP *in vitro*. In B95a cells, both IC323-EGFP and EdH-EGFP induced large syncytia and strong EGFP expression, whereas in Vero cells, only EdH-EGFP induced syncytia and strong EGFP expression (Fig. 1B), consistent with our previous observation (35). Notably, EdH-EGFP induced large syncytia and strong EGFP expression in primary kidney and primary astroglial cells derived from cynomolgus monkey tissues (Fig. 1B). Thus, the H protein of the Edmonston vaccine strain of MV can expand the *in vitro* cell specificity of the wild-type MV strain in established cell lines as well as in primary cell cultures of cynomolgus monkey tissues.

Preliminary infection of cynomolgus monkeys with recombinant MV strains. We next examined the *in vivo* tropism and growth of IC323-EGFP$_2$ and EdH-EGFP$_2$ by using 3 cynomolgus

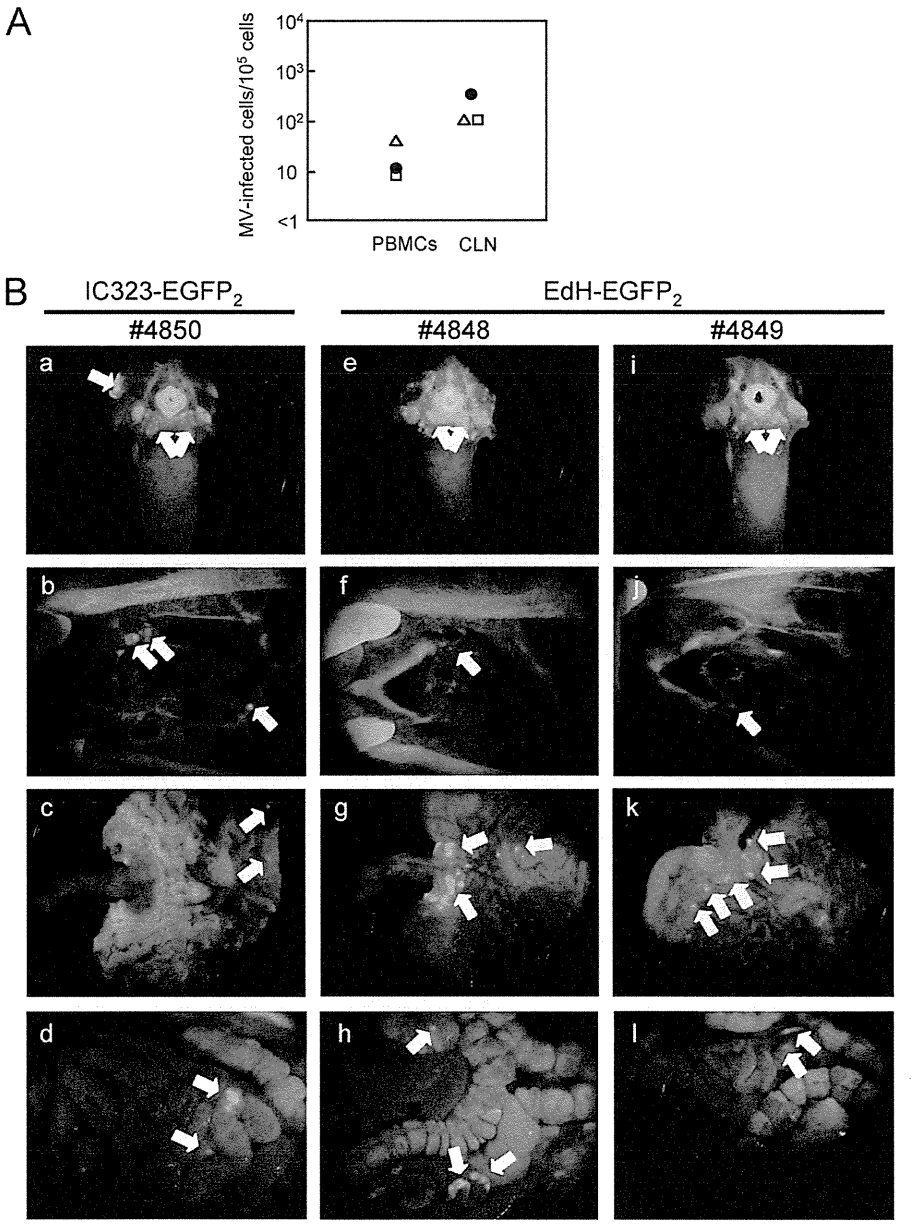

FIG 2 Detection of MV-infected cells in peripheral blood mononuclear cells (PBMCs) and cervical lymph nodes and EGFP expression in the tissues and organs of infected macaques. (A) One monkey (no. 4850) (closed circles) was infected with IC323-EGFP$_2$ and 2 monkeys (no. 4848 and 4849) (open triangles and open squares, respectively) were infected with EdH-EGFP$_2$. Single-cell suspensions (10^5/ml) from PBMCs and cervical lymph nodes (CLN) were divided into 2-fold serial dilutions, and then a 1-ml aliquot of each diluted single-cell suspension was inoculated into subconfluent B95a cells on 24-well cluster plates in duplicate. The number of MV-infected cells per 10^5 single-cell suspensions was then calculated. (B) At day 7, EGFP fluorescence in the tongue and tonsils (a, e, and i), cervical lymph nodes (b, f, and j), stomach (c, g, and k), and gut-associated lymph nodes (d, h, and l) was detected using a fluorescence microscope with a charge-coupled device (CCD) camera. Arrows indicate the MV-infected regions expressing EGFP.

monkeys. Prior to the infection of monkeys with IC323-EGFP$_2$ and EdH-EGFP$_2$, we examined the *in vitro* cell specificities of the two strains by using B95a and Vero cells and confirmed that EdH-EGFP$_2$ had the wider *in vitro* cell specificity (Fig. 1C). Then, one monkey (no. 4850) was inoculated with IC323-EGFP$_2$, and two monkeys (no. 4848 and 4849) were inoculated with EdH-EGFP$_2$. At day 7, viremia was observed in all 3 monkeys (Fig. 2A). Upon necropsy at day 7, nearly the same numbers of MV-infected cells were isolated from the cervical lymph nodes of the 3 monkeys (Fig. 2A). EGFP fluorescence was observed in many lymphoid tissues, including the cervical lymph nodes, tongue, tonsils, stomach, and gut-associated lymph nodes, in the 3 monkeys (Fig. 2B). No sig-

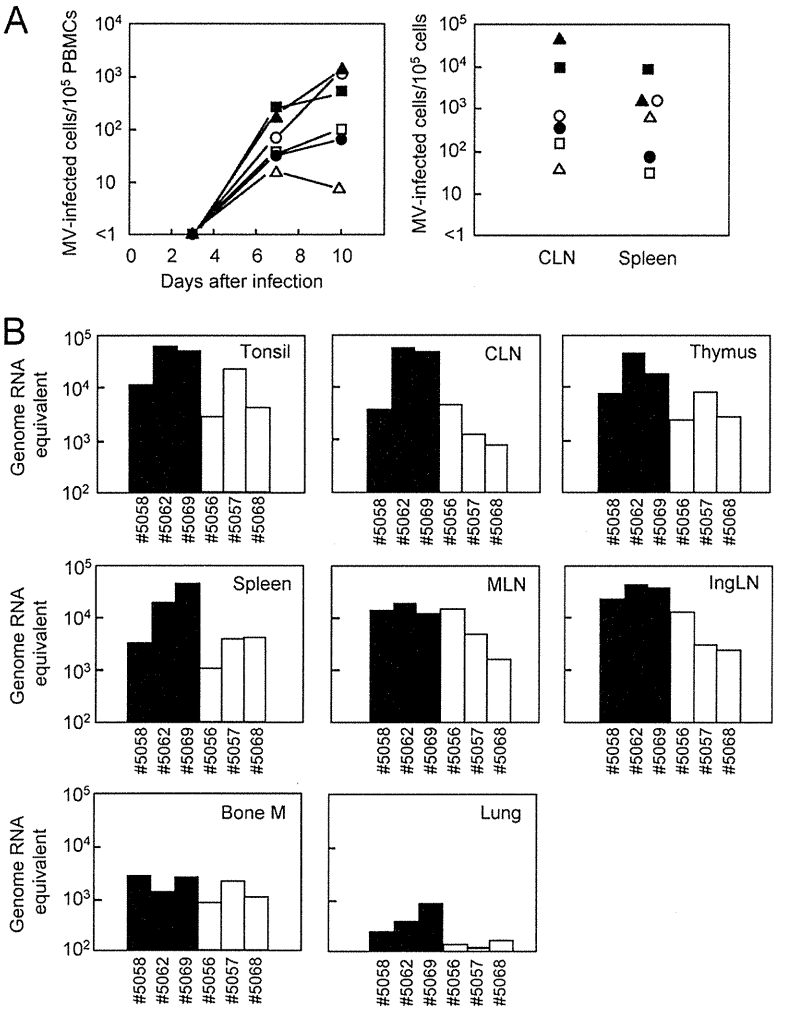

FIG 3 Detection of MV-infected cells and MV genome RNA. (A) Three monkeys (no. 5058, 5062, and 5069) (closed circles, closed triangles, and closed squares, respectively) were infected with IC323-EGFP$_2$, and 3 monkeys (no. 5056, 5057, and 5068) (open circles, open triangles, and open squares, respectively) were infected with EdH-EGFP$_2$. PBMCs were obtained at days 3, 7, and 10. CLN and spleens were obtained on day 10. Single-cell suspensions (10^5/ml) from PBMCs, CLN, and spleen were divided into 2-fold serial dilutions, and then a 1-ml aliquot of each diluted single-cell suspension was inoculated into subconfluent B95a cells on 24-well cluster plates in duplicate. The number of MV-infected cells per 10^5 single-cell suspensions was then calculated. (B) MV genome RNA was detected by real-time reverse transcription-PCR on total RNA isolated from tonsils, CLN, thymus, spleens, mesenteric lymph nodes (MLN), inguinal lymph nodes (IngLN), bone marrow (bone M), and lungs. Three monkeys (no. 5058, 5062 and 5069) were infected with IC323-EGFP$_2$, and 3 monkeys (no. 5056, 5057, and 5068) were infected with EdH-EGFP$_2$. The results for the real-time RT-PCR were expressed as genome RNA equivalent to plasmid p(+)MV323-EGFP.

nificant difference in the distributions and intensities of EGFP fluorescence in the internal organs and tissues was observed among the 3 monkeys, indicating that the tropism of EdH-EGFP$_2$ was not expanded *in vivo*.

Growth of recombinant MV strains in cynomolgus monkeys. To assess whether these results could be confirmed, 6 monkeys were infected with IC323-EGFP$_2$ or EdH-EGFP$_2$. Three monkeys (no. 5058, 5062, and 5069) were inoculated with IC323-EGFP$_2$, and 3 monkeys (no. 5056, 5057, and 5068) were inoculated with EdH-EGFP$_2$. At day 7, viremia was detected in all 6 monkeys, and the number of infected cells was increased at day 10 in most monkeys (Fig. 3A, left). Upon necropsy at day 10, MV-infected cells were isolated from the cervical lymph nodes and spleens of the 6 monkeys (Fig. 3A, right). In monkeys infected with IC323-EGFP$_2$ a large number of the lymphocytes (up to 49%) of cervical lymph nodes were infected, whereas in monkeys infected with EdH-EGFP$_2$, a smaller number (0.040 to 0.77%) of the lymphocytes of cervical lymph nodes were infected (Fig. 3A, right). Similarly, in monkeys infected with IC323-EGFP$_2$, a large number of the lymphocytes (up to 8.2%) in the spleen were infected, whereas in monkeys infected with EdH-EGFP$_2$, a smaller number (0.032 to 1.5%) of the lymphocytes in cervical lymph nodes were infected (Fig. 3A, right). In all 6 monkeys infected with either IC323-EGFP$_2$ or EdH-EGFP$_2$, substantial amounts of MV genome RNA were detected in the tonsils, cervical lymph nodes, thymus, spleen, mesenteric lymph nodes, inguinal lymph nodes, bone marrow,

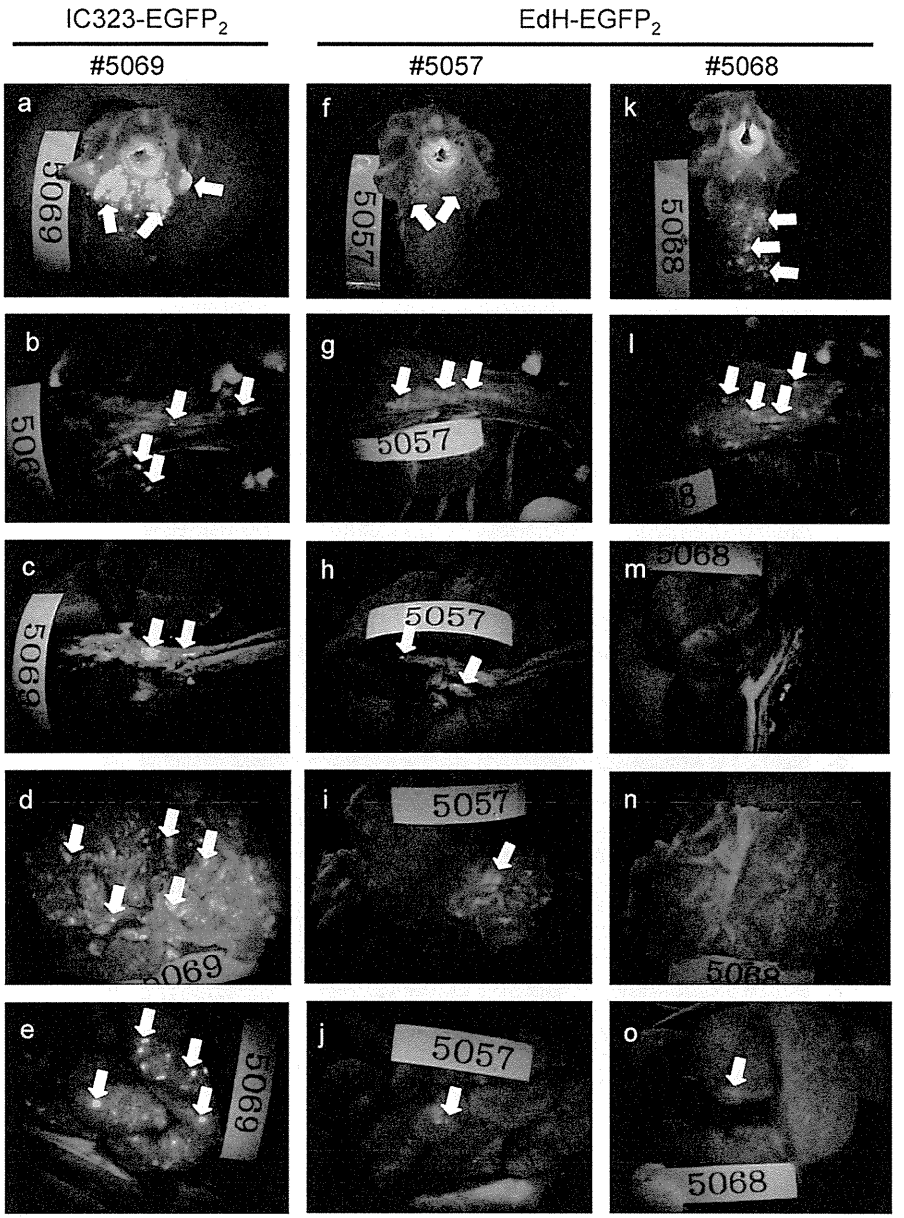

FIG 4 EGFP expression in tissues of monkeys after experimental infection with IC323-EGFP$_2$ and EdH-EGFP$_2$. At day 10, EGFP fluorescence in the tongue and tonsils (a, f, and k), thymus (b, g, and l), trachea and lung (c, h, and m), stomach (d, i, and n), and gut-associated lymph nodes (e, j, and o) of infected monkeys was detected using a fluorescence microscope with a CCD camera.

and lungs (Fig. 3B). We note that the amount of MV genome RNA in EdH-EGFP$_2$-infected monkeys was significantly lower than that in IC323-EGFP$_2$-infected monkeys, especially in lungs.

Macroscopic detection of EGFP fluorescence in organs and tissues. In all 6 monkeys infected by IC323-EGFP$_2$ or EdH-EGFP$_2$, EGFP fluorescence was macroscopically detected in many lymphoid organs and tissues, including the tongue and tonsils, thymus, trachea and lungs, stomach, and gut-associated lymph nodes, upon necropsy at day 10 (Fig. 4). No difference in the distribution of EGFP fluorescence in the internal organs and tissues was observed between monkeys infected with IC323-EGFP$_2$ or EdH-EGFP$_2$, confirming that tropism of EdH-EGFP$_2$ is not expanded in macaques. However, the intensity of EGFP fluorescence in the internal organs and tissues of EdH-EGFP$_2$-infected monkeys was significantly weaker than that in IC323-EGFP$_2$-infected monkeys.

Histopathological and immunohistochemical analyses. To further examine the tissue and organ tropism of IC323-EGFP$_2$ and EdH-EGFP$_2$, we performed histopathological and immunohistochemical analyses of fixed specimens. In bronchioles, we histo-

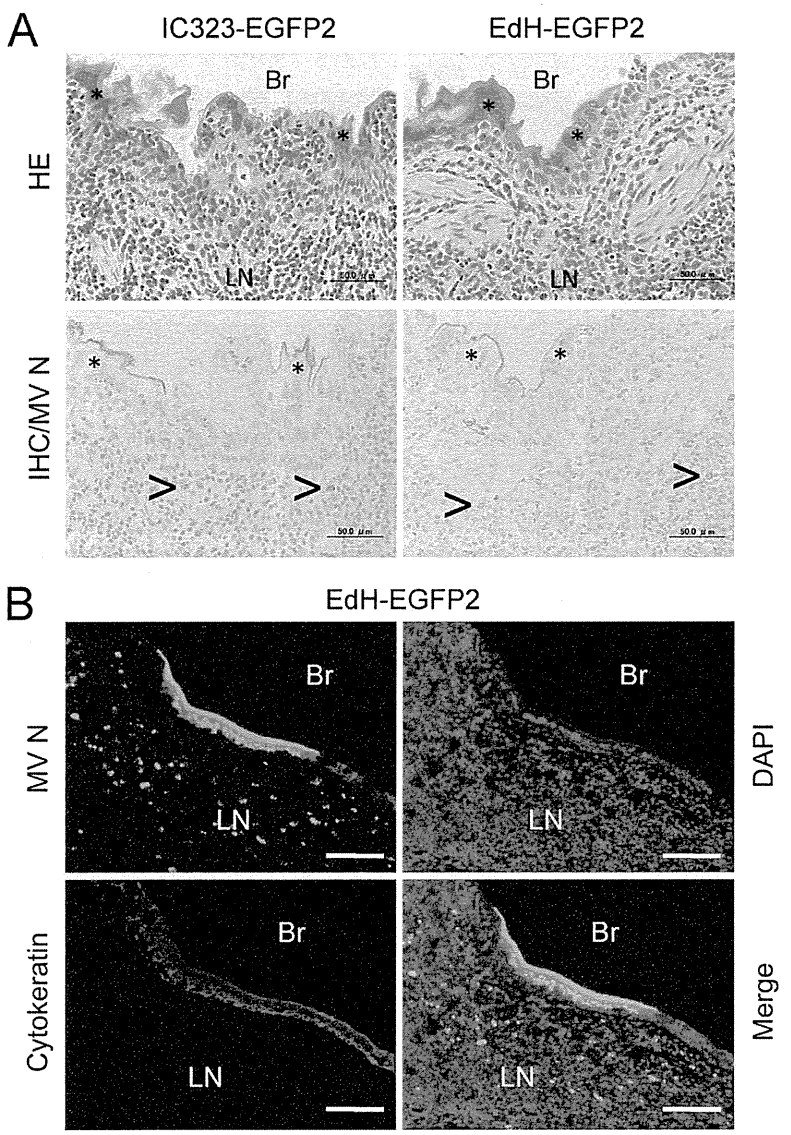

FIG 5 Histopathological and immunohistochemical analyses. (A) Bronchiole sections obtained from monkeys infected with IC323-EGFP$_2$ or EdH-EGFP$_2$ were examined by hematoxylin and eosin staining and immunohistochemistry. Giant-cell formation (*) and lymphoid filtrates were seen in the epithelial layer of the bronchiole. MV nucleocapsid (N) antigen (light brown) was detected in the cytoplasm and nucleus in the giant cells and in the cytoplasm of the lymphocytes (arrows) of lymphatic nodules under the epithelial layer by immunohistochemical analysis (IHC). (B) The bronchiole area obtained from a monkey infected with EdH-EGFP$_2$ was investigated by double immunofluorescence staining. Tissue sections were stained with antiserum against the MV N antigen and mouse monoclonal antibody against cytokeratin. DAPI was used to identify nuclei. Br, bronchiole; LN, lymphatic nodule. Bars, 50 μm (A) and 100 μm (B).

pathologically observed bronchiolitis and giant cells with eosinophilic inclusion bodies in monkeys infected with both IC323-EGFP$_2$ and EdH-EGFP$_2$, and MV N antigen was detected in both sections (Fig. 5A). Tissue sections obtained from the bronchiole area were double stained with anti-MV N and anticytokeratin antibodies, which clearly showed infection of EdH-EGFP$_2$ in the epithelial cells (Fig. 5B) as reported for wild-type MV (3, 20), possibly through a nectin-4-mediated pathway (18, 20, 23, 31). Interestingly, the N protein was accumulated under the apical plasma membrane of the infected cells (Fig. 5B), suggesting an intracellular mechanism of transport of the N protein to the apical plasma membrane. The MV N antigen was detected in the lymphocytes of the spleen, mesenteric and cervical lymph nodes, thymus, salivary gland, tonsils, stomach, and jejunum (Table 1), as well as in epithelia of the lungs, bronchi, tonsils, and stomach, but not in the muscles of the heart and in the epithelia of the liver, kidney, skin, tonsils, and stomach of most monkeys. These data again indicated that tropism of EdH-EGFP$_2$ was not expanded in macaques.

Flow cytometric analysis. To examine the cell tropism of IC323-EGFP$_2$ and EdH-EGFP$_2$ in lymphocytes, EGFP expression in lymphocytes isolated from PBMCs and mesenteric lymph

TABLE 1 Detection of giant cells and measles virus nucleocapsid antigen in different tissues by immunohistochemistry

Organ	Tissue or cell type	Detection of giant cells or antigens after: IC323-EGFP$_2$ infection of monkey no.: 5058 Giant cells	5058 Viral antigens	5062 Giant cells	5062 Viral antigens	5069 Giant cells	5069 Viral antigens	EdH-EGFP$_2$ infection of monkey no.: 5056 Giant cells	5056 Viral antigens	5057 Giant cells	5057 Viral antigens	5068 Giant cells	5068 Viral antigens
Lung	Epithelium	+	+	+	+	+	+	+	+	+	+	+	+
Bronchus	Epithelium	+	+	+	+	+	+	+	−	+	+	+	+
Heart	Muscle	−	−	−	−	−	−	−	−	−	−	−	−
Liver	Epithelium	−	−	−	+	−	−	−	−	−	−	−	−
Kidney	Epithelium	−	−	+	+	−	−	−	−	−	+	−	−
Skin	Epithelium	−	−	+	+	−	−	−	−	−	−	+	+
Spleen	Lymphocyte	+	+	+	+	+	+	+	+	+	+	−	−
Mesenteric lymph node	Lymphocyte	+	+	+	+	+	+	+	+	+	+	+	+
Cervical lymph node	Lymphocyte	+	+	+	+	+	+	+	+	+	+	+	+
Thymus	Lymphocyte	+	+	+	+	+	+	+	+	+	+	+	+
Salivary gland	Lymphocyte	−	−	−	+	−	+	−	+	−	+	−	+
Tonsil	Epithelium	NE[a]	NE	+	+	+	+	+	+	NE	NE	+	+
	Lymphocyte	NE	NE	+	+	+	+	+	+	NE	NE	+	+
Stomach	Epithelium	−	−	+	+	+	+	+	+	−	−	+	+
	Lymphocyte	−	+	−	+	−	+	−	+	−	+	−	+
Pancreas	Epithelium	−	−	−	−	−	−	−	−	−	−	−	−
Jejunum	Lymphocyte	−	+	−	+	−	+	−	+	−	+	−	+

[a] NE, not examined.

nodes was analyzed by flow cytometry. A total of 0.90% and 8.59% of B lymphocytes in PBMCs and MLNs, respectively, and 0.90% and 3.90% of T lymphocytes in PBMCs and MLNs, respectively, were infected with IC323-EGFP$_2$ (Fig. 6). Lymphocytes expressing SLAM were infected with IC323-EGFP$_2$, as previously reported (3). Similarly, 0.44 to 0.53% and 1.06 to 2.23% of B lymphocytes in PBMCs and MLNs, respectively, and 0.42 to 0.68% and 0.70 to 1.44% of T lymphocytes in PBMCs and MLNs, respectively, were infected with EdH-EGFP$_2$ (Fig. 6). Lymphocytes expressing SLAM were also infected with EdH-EGFP$_2$. These results indicated that tropism of EdH-EGFP$_2$ was not expanded in lymphocytes of macaques. Interestingly, the number and intensity of EGFP-expressing cells in lymphocytes of EdH-EGFP$_2$-infected monkeys were significantly lower than those in of IC323-EGFP$_2$-infected monkeys.

Cytokine production by infected monkeys. To investigate whether the differences in growth of IC323-EGFP$_2$ and EdH-EGFP$_2$ in monkeys were associated with altered host responses to infection, we measured cytokine and chemokine levels in plasma samples from infected monkeys. The cytokines selected for analysis were IL-12, IFN-γ, IL-2, IL-4, IL-5, and IL-17 (Th1/Th2 balance) and the IL-6, TNF-α, IL-1β, and MCP-1 (inflammatory response).

With Th1-type cytokines, we found that plasma levels of IL-12 were high for 3 (no. 5056, 5057, and 5062) out of 6 monkeys at day 0, were slightly elevated at day 3, and then declined by day 7 (Fig. 7). The plasma levels of IL-12 for the 3 other monkeys (no. 5058, 5068, and 5069) were low throughout the experiment. Irrespective of the plasma levels of IL-12, the plasma levels of IFN-γ were elevated in all 6 monkeys. The increase in plasma levels of IL-2 was marginal by day 10 for 5 monkeys. For inflammatory cytokines, the plasma level of MCP-1 was markedly elevated for all monkeys. IL-4, IL-17, and IL-1β were not detected throughout the experiment. Other cytokines (IL-5, IL-6, and TNF-α) were not consistently detected (data not shown).

Taking the results together, there were no significant differences in the cytokine production profiles of the monkeys infected with IC323-EGFP$_2$ or EdH-EGFP$_2$, and similar Th1-type and inflammatory responses against acute MV infection occurred in monkeys infected with IC323-EGFP$_2$ or EdH-EGFP$_2$.

DISCUSSION

In this study, we compared the cell specificities and tropisms of the wild-type strains of MV bearing the H protein of the Edmonston vaccine strain with those of the wild-type MV strains. Although EdH-EGFP showed wider cell specificity in cell lines and primary cell cultures (Fig. 1B), the tissue and organ tropism of EdH-EGFP$_2$ was not altered in all 5 infected macaques (Fig. 2 and 4 and Table 1). Since CD46 is ubiquitously expressed in human and monkey cells, EdH-EGFP$_2$ could infect all cells in macaques. However, widespread infection of EdH-EGFP$_2$ in tissues and organs was not observed. This result is not surprising because it was reported that only the lymph nodes and spleen of monkeys were infected with MV vaccine strains (39). Furthermore, it was recently reported that CD11c-positive myeloid cells, such as alveolar macrophages and dendritic cells in lungs of monkeys, were infected with an EGFP-expressing recombinant Edmonston strain of MV via an aerosol route (5). This result is consistent with our findings in that the CD46-using Edmonston vaccine strain does not cause widespread infection in the lungs of monkeys, although there is a possibility that the infection by the Edmonston strain in lungs may be restricted due to mutations in the N and P/C/V genes, which are most important in combating the innate immune system.

One possible explanation for the limited infection of EdH-EGFP$_2$ in macaques is the expression level of CD46. Anderson et al. reported that at low CD46 density, infection with the MV vac-

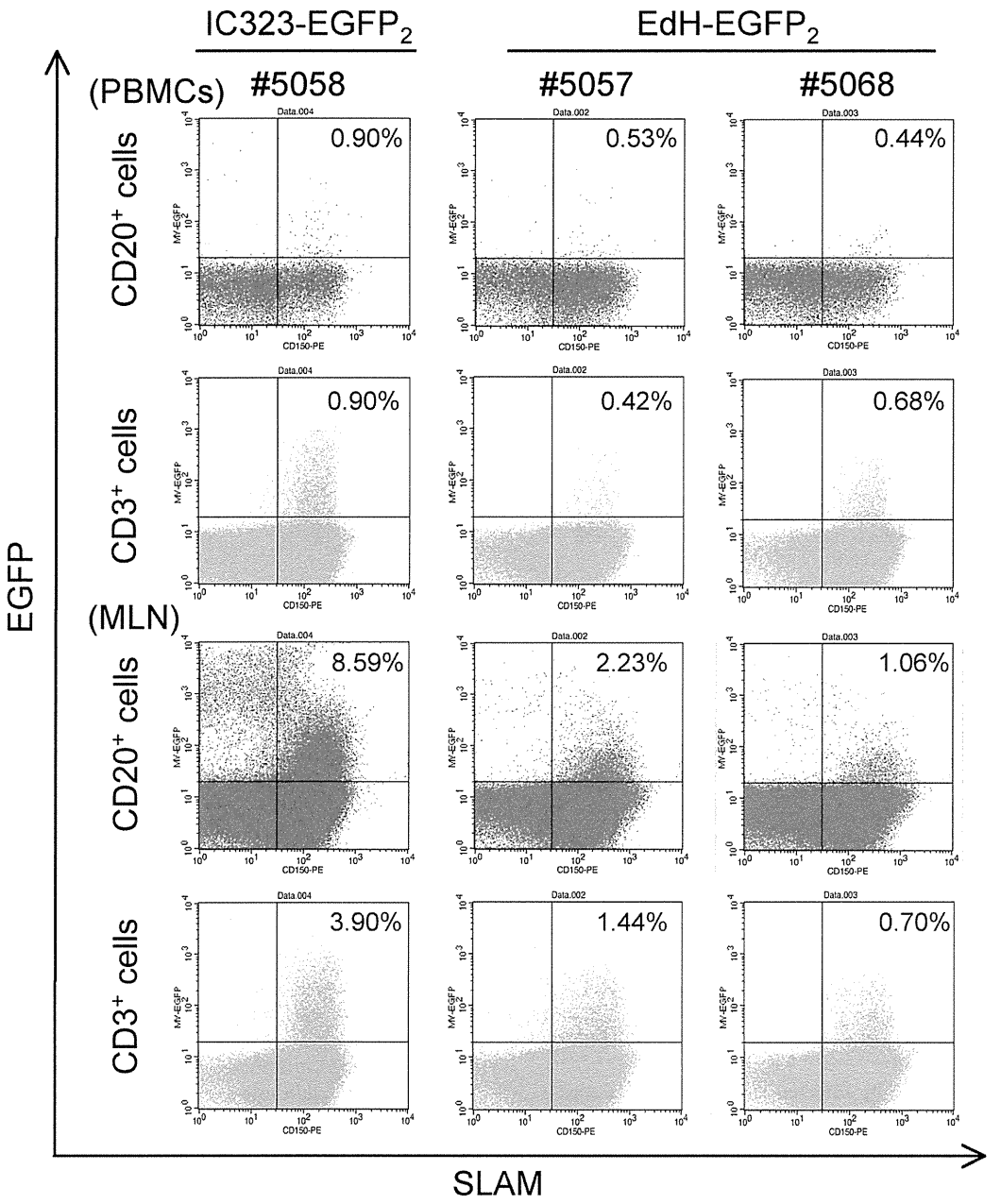

FIG 6 EGFP-positive cells in lymphocyte subpopulations of PBMCs and mesenteric lymph nodes from infected monkeys. Cryopreserved PBMCs and mesenteric lymph nodes (MLN) of monkeys infected with IC323-EGFP$_2$ (no. 5058) or EdH-EGFP$_2$ (no. 5057 and 5068) were stained with monoclonal antibodies against CD3, CD20, and CD150 (signaling lymphocyte activation molecule [SLAM]) and analyzed with a FACSCalibur instrument. Results are shown as dot plots, with SLAM expression on the *x* axis and EGFP expression on the *y* axis. EGFP expression in CD20$^+$ B lymphocytes and CD3$^+$ T lymphocytes is shown. CD46 expression in lymphocytes of PBMCs of monkeys infected with EdH-EGFP$_2$ (no. 5057 and 5068) was detected with monoclonal antibody against CD46 and isotype control antibody.

cine strain occurs but subsequent cell-to-cell fusion does not (1). If the expression levels of CD46 are low in cells in the tissues, EdH-EGFP$_2$ may infect those cells, but subsequent cell-to-cell fusion may not occur. In primary cell cultures, gene expression profiles often change when tissue cells are cultured *in vitro*. Thus, it is likely that the CD46 expression levels of primary cell cultures are high enough for infection with EdH-EGFP. We are now examining the expression levels of CD46 in cell lines and primary cell cultures and in tissues of cynomolgus monkeys. Another possible explanation for the limited infection of EdH-EGFP$_2$ in macaque tissues is the inefficient replication of MV due to interferons. Yoshikawa et al. reported that primate kidney cells rapidly lose

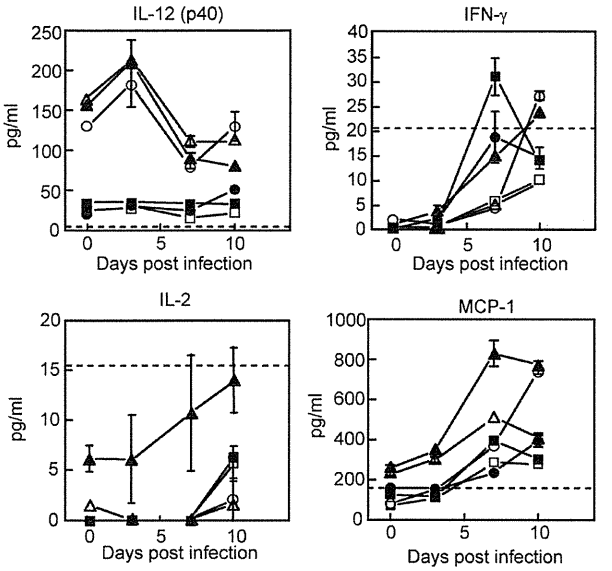

FIG 7 Detection of cytokines in plasma samples from infected monkeys. Three monkeys (no. 5058, 5062, and 5069) (closed circles, closed triangles, and closed squares, respectively) were infected with IC323-EGFP$_2$. Three other monkeys (no. 5056, 5057, and 5068) (open circles, open triangles, and open squares, respectively) were infected with EdH-EGFP$_2$. Plasma was obtained at days 0, 3, 7, and 10. Cytokine levels in the plasma were measured with a Luminex 200 instrument using a Milliplex nonhuman primate cytokine/chemokine kit. The physiological upper concentration ranges detected in human plasma are indicated by dotted lines.

interferon-inducing activity and permit poliovirus replication when the cells are cultured *in vitro* (40). MV replication in monkey tissues may be inhibited by interferon, whereas MV replication in primary cell cultures can occur due to the lack of interferon-inducing activity.

Flow cytometric analysis showed that lymphocytes expressing SLAM were infected with both IC323-EGFP$_2$ and EdH-EGFP$_2$ (Fig. 6). It is known that stimulated lymphocytes can be efficiently infected with MV and that SLAM is highly expressed in stimulated lymphocytes (11). Thus, the activation status of lymphocytes may be important for infection with MV, and infection of unstimulated lymphocytes with EdH-EGFP$_2$ by the CD46-mediated pathway would not result in efficient MV replication. As a result, lymphocytes expressing SLAM may appear to be equally infected with both strains. Recently, two groups revealed that both SLAM and CD46 are required for stable transduction of resting human lymphocytes with lentiviral vectors pseudotyped with the vaccine MV F and H proteins (8, 42). Thus, another possibility is that SLAM binding in addition to CD46 binding may be required for efficient infection of lymphocytes with EdH-EGFP$_2$. SLAM binding and subsequent signaling (8, 42) may be important for efficient MV infection.

A previous study in which monkeys were infected with pathogenic and Edmonston vaccine strains via an aerosol route showed that only the pathogenic strain caused massive infection in lymphoid tissues (5). We also infected monkeys with IC323-EGFP$_2$ and EdH-EGFP$_2$ via the aerosol route, and we found that both strains caused massive infection in lymphoid tissues (Fig. 3). This result indicated that the Edmonston H protein does not influence the extent of infection in lymphoid tissues. Proteins other than the H protein, possibly viral polymerase proteins (30), may regulate MV replication in lymphoid tissues.

Suppression of the production of IL-12 during measles was proposed (10). We found that the initial level of IL-12 was high for 3 monkeys (no. 5056, 5057, and 5062) but low for 3 other monkeys (no. 5058, 5068, and 5069) (Fig. 7). We do not have an explanation for this difference. However, our results indicated that the IL-12 levels were not significantly induced at early time points during MV infection. This result may be consistent with a previous observation of suppressed serum levels of IL-12 during MV infection in rhesus macaques (13, 26). Interestingly, Th1-type cytokines (IFN-γ and IL-2) were induced in all monkeys irrespective of the IL-12 level. The induction of IFN-γ in plasma at early time points is consistent with that in previous studies of human measles (10, 19, 24, 41). A previous study showed no significant induction of IL-2, IL-12, and IFN-γ in monkeys infected with wild-type MV (4). However, in that experiment the induction of IL-2, IL-12, and IFN-γ was measured by quantitating their mRNAs by real-time RT-PCR using RNA extracted from PBMCs. Real-time RT-PCR data may not coincide with the actual amounts of cytokines in plasma.

In summary, the current study showed that the H protein of the Edmonston vaccine strain alters the cell specificity of wild-type MV *in vitro* but not the tropism in macaques. SLAM$^+$ cells were main target for both IC323-EGFP$_2$ and EdH-EGFP$_2$ in macaques. In addition, it is suggested that the Edmonston vaccine H protein attenuates MV growth *in vivo*, especially at a later stage. It has long been proposed that the vaccine H protein attenuates the virus growth *in vivo* by several mechanisms (e.g., CD46-mediated signaling in infected cells or downregulation of CD46 in infected cells and subsequent complement-mediated cell lysis) (14). It will be interesting to examine the type I interferon production and the downregulation of CD46 in MV-infected cells in monkeys infected with EdH-EGFP$_2$ or MV vaccine strains.

ACKNOWLEDGMENTS

We thank Y. Yanagi and M. Takeda for providing plasmids and cells, B. Moss for vaccinia virus vTF7-3, N. Kimura for primary monkey astroglial cells, A. Harashima, M. Fujino, H. Sato, Y. Saito, A. Wakutsu, K. Kato, and T. Nishie for excellent technical support, and Y. Yasutomi, K. Terao, A. Yamada, T. Sata, H. Hasegawa, and K. Komase for valuable discussions and continuous support. We also thank K. Ho for critical readings and valuable comments.

This work was supported in part by a grant-in-aid (no. 21022006 and 23659227) from the Ministry of Education, Culture, Sports, Science and Technology of Japan.

REFERENCES

1. **Anderson BD, Nakamura T, Russell SJ, Peng K-W.** 2004. High CD46 receptor density determines preferential killing of tumor cells by oncolytic measles virus. Cancer Res. 64:4919–4926.
2. **Auwaerter PG, et al.** 1999. Measles virus infection in rhesus macaques: altered immune responses and comparison of the virulence of six different virus strains. J. Infect. Dis. 180:950–958.
3. **de Swart RL, et al.** 2007. Predominant infection of CD150+ lymphocytes and dendritic cells during measles virus infection of macaques. PLoS Pathog. 3:e178.
4. **Devaux P, Hodge G, McChesney MB, Cattaneo R.** 2008. Attenuation of V- or C-defective measles viruses: infection control by the inflammatory and interferon responses of rhesus monkeys. J. Virol. 82:5359–5367.
5. **de Vries RD, et al.** 2010. In vitro tropism of attenuated and pathogenic measles virus expressing green fluorescent protein in macaques. J. Virol. 84:4714–4724.

6. **Dorig RE, Marcil A, Chopra A, Richardson CD.** 1993. The human CD46 molecule is a receptor for measles virus (Edmonston strain). Cell **75**:295–305.
7. **Enders JF, Peebles TC.** 1954. Propagation in tissue cultures of cytopathic agents from patients with measles. Proc. Soc. Exp. Biol. Med. **86**:277–286.
8. **Frecha C, et al.** 2011. Measles virus glycoprotein-pseudotyped lentiviral vector-mediated gene transfer into quiescent lymphocytes requires binding to both SLAM and CD46 entry receptors. J. Virol. **85**:5975–5985.
9. **Fuerst TR, Niles EG, Studier FW, Moss B.** 1986. Eukaryotic transient-expression system based on recombinant vaccinia virus that synthesizes bacteriophage T7 RNA polymerase. Proc. Natl. Acad. Sci. U. S. A. **83**: 8122–8126.
10. **Griffin DE, Ward BJ, Jauregui E, Johnson RT, Vaisberg A.** 1990. Immune activation during measles: interferon-γ and neopterin in plasma and cerebrospinal fluid in complicated and uncomplicated disease. J. Infect. Dis. **161**:449–453.
11. **Griffin DE.** 2007. Measles virus, p 1551–1585. *In* Knipe DM, Howley PM, Griffin DE, Lamb RA, Martin MA, Roizman B, Straus SE (ed), Fields virology, 5th ed. Lippincott Williams & Wilkins, Philadelphia, PA.
12. **Hashimoto K, et al.** 2002. SLAM (CD150)-independent measles virus entry as revealed by recombinant virus expressing green fluorescent protein. J. Virol. **76**:6743–6749.
13. **Hoffman SJ, et al.** 2003. Vaccination of rhesus macaques with a recombinant measles virus expressing interleukin-12 alters humoral and cellular immune responses. J. Infect. Dis. **188**:1553–1561.
14. **Kemper C, Atkinson JP.** 2009. Measles virus and CD46. Curr. Top. Microbiol. Immunol. **329**:31–57.
15. **Kobune F, Sakata H, Sugiura A.** 1990. Marmoset lymphoblastoid cells as a sensitive host for isolation of measles virus. J. Virol. **64**:700–705.
16. **Kobune F, et al.** 1996. Nonhuman primate models of measles. Lab. Anim. Sci. **46**:315–320.
17. **Lamb RA, Parks GD.** 2007. *Paramyxoviridae*: the viruses and their replication, p 1449–1496. *In* Knipe DM, Howley PM, Griffin DE, Lamb RA, Martin MA, Roizman B, Straus SE (ed), Fields virology, 5th ed. Lippincott Williams & Wilkins, Philadelphia, PA.
18. **Leonard VHJ, et al.** 2008. Measles virus blind to its epithelial cell receptor remains virulent in rhesus monkeys but cannot cross the airway epithelium and is not shed. J. Clin. Invest. **118**:2448–2458.
19. **Moss WJ, Ryon JJ, Monze M, Griffin DE.** 2002. Differential regulation of interleukin (IL)-4, IL-5, and IL-10 during measles in Zambian children. J. Infect. Dis. **186**:879–887.
20. **Muhlebach MD, et al.** 2011. Adherens junction protein nectin-4 is the epithelial receptor for measles virus. Nature **480**:530–533.
21. **Naniche D, et al.** 1993. Human membrane cofactor protein (CD46) acts as a cellular receptor for measles virus. J. Virol. **67**:6025–6032.
22. **Navaratnarajah C, Leonard KVHJ, Cattaneo R.** 2009. Measles virus glycoprotein complex assembly, receptor attachment, and cell entry. Curr. Top. Microbiol. Immunol. **330**:59–76.
23. **Noyce RS, et al.** Tumor cell marker PVRL4 (nectin 4) is an epithelial cell receptor for measles virus. ProS Pahog. 7:e1002240.
24. **Ohga S, Miyazaki C, Okada K, Akazawa K, Ueda K.** 1992. The inflammatory cytokines in measles: correlation between serum interferon-γ levels and lymphocyte subpopulations. Eur. J. Pediatr. **151**:492–496.
25. **Plumet S, Gerlier D.** 2005. Optimized SYBR green real-time PCR assay to quantify the absolute copy number of measles virus RNAs using gene specific primers. J. Virol. Methods **128**:79–87.
26. **Polack FP, Hoffman SJ, Moss WJ, Griffin DE.** 2002. Altered synthesis of interleukin-12 and type 1 and type 2 cytokines in rhesus macaques during measles and atypical measles. J. Infect. Dis. **185**:13–19.
27. **Rota JS, Wang ZD, Rota PA, Bellini WJ.** 1994. Comparison of sequences of the H, F, and N coding genes of measles virus vaccine strains. Virus Res. **31**:317–330.
28. **Tahara M, Takeda M, Seki F, Hashiguchi T, Yanagi Y.** 2007. Multiple amino acid substitutions in hemagglutinin are necessary for wild-type measles virus to acquire the ability to use receptor CD46 efficiently. J. Virol. **81**:2564–2572.
29. **Takeda M, et al.** 2005. Efficient rescue of measles virus from cloned cDNA using SLAM-expressing Chinese hamster ovary cells. Virus Res. **108**:161–165.
30. **Takeda M, et al.** 2008. Measles viruses possessing the polymerase protein genes of the Edmonston vaccine strain exhibit attenuated gene expression and growth in cultured cells and SLAM knock-in mice. J. Virol. **82**:11979–11984.
31. **Takeda M, et al.** 2007. A human lung carcinoma cell line supports efficient measles virus growth and syncytium formation via a SLAM- and CD46-independent mechanism. J. Virol. **81**:12091–12096.
32. **Takeda M, et al.** 2000. Recovery of pathogenic measles virus from cloned cDNA. J. Virol. **74**:6643–6647.
33. **Takeuchi K, Miyajima N, Kobune F, Tashiro M.** 2000. Comparative nucleotide sequence analyses of the entire genomes of B95a cell-isolated and Vero cell-isolated measles viruses from the same patient. Virus Genes **20**:253–257.
34. **Takeuchi K, et al.** 2005. Stringent requirement for the C protein of wild-type measles virus for growth in vitro and in macaques. J. Virol. **79**:7838–7844.
35. **Takeuchi K, et al.** 2002. Recombinant wild-type and Edmonston strain measles viruses bearing heterologous H proteins: role of H protein in cell fusion and host cell specificity. J. Virol. **76**:4891–4900.
36. **Tatsuo H, Ono N, Tanaka K, Yanagi Y.** 2000. SLAM (CDw150) is a cellular receptor for measles virus. Nature **406**:893–897.
37. **van Binnendijk RS, van der Heijden RW, van Amerongen G, Uytde-Haag FG, Osterhaus AD.** 1994. Viral replication and development of specific immunity in macaques after infection with different measles virus strains. J. Infect. Dis. **170**:443–448.
38. **von Messling V, Milosevic D, Cattaneo R.** 2004. Tropism illuminated: lymphocyte-based pathways blazed by lethal morbillivirus through the host immune system. Proc. Natl. Acad. Sci. U. S. A. **101**:14216–14221.
39. **Yamanouchi K, et al.** 1970. Giant cell formation in lymphoid tissue of monkeys inoculated with various strains of measles virus. Jpn. J. Med. Sci. Biol. **23**:131–145.
40. **Yoshikawa T, et al.** 2006. Role of the alpha/beta interferon response in the acquisition of susceptibility to poliovirus by kidney cells in culture. J. Virol. **80**:4313–4325.
41. **Yu X, et al.** 2008. Measles virus infection in adults induces production of IL-10 and is associated with increased CD4+CD25+ regulatory T cells. J. Immunol. **181**:7356–7366.
42. **Zhou Q, Schneider IC, Gallet M, Kneissl S, Buchholz CJ.** 2011. Resting lymphocyte transduction with measles virus glycoprotein pseudotyped lentiviral vectors relies on CD46 and SLAM. Virology **413**:149–152.

JOURNAL OF NATURAL PRODUCTS

Note

pubs.acs.org/jnp

Trichostatin Analogues JBIR-109, JBIR-110, and JBIR-111 from the Marine Sponge-Derived *Streptomyces* sp. RM72

Takahiro Hosoya,[†] Takatsugu Hirokawa,[‡] Motoki Takagi,*[,†] and Kazuo Shin-ya*[,§]

[†]Biomedicinal Information Research Center (BIRC), Japan Biological Informatics Consortium (JBIC), 2-4-7 Aomi, Koto-ku, Tokyo 135-0064, Japan

[‡]Computational Biology Research Center (CBRC), National Institute of Advanced Industrial Science and Technology (AIST), 2-4-7 Aomi, Koto-ku, Tokyo 135-0064, Japan

[§]Biomedicinal Information Research Center (BIRC), National Institute of Advanced Industrial Science and Technology (AIST), 2-4-7 Aomi, Koto-ku, Tokyo 135-0064, Japan

Supporting Information

ABSTRACT: Three new trichostatin analogues, JBIR-109 (**1**), JBIR-110 (**2**), and JBIR-111 (**3**), were isolated from the culture of the marine sponge-derived *Streptomyces* sp. strain RM72, together with trichostatin A (**4**) and trichostatic acid (**5**). The planar structures of **1**−**3** were determined on the basis of extensive NMR and MS analyses. In addition, the absolute configurations of the amino acid residues were determined by Marfey's method. The histone deacetylase inhibitory activities of **1**−**5** were examined, and their structure−activity relationships are discussed.

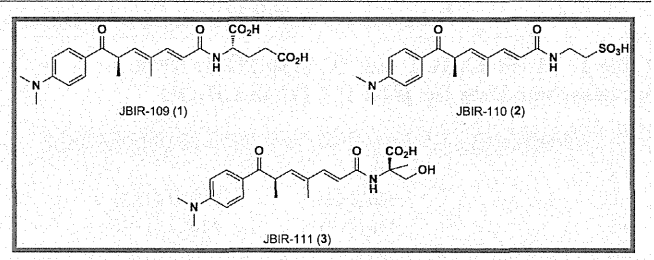

Histone deacetylases (HDACs) play an important role in the epigenetic regulation of gene expression by catalyzing the deacetylation of lysine residues in histone proteins, stimulating chromatin condensation, and promoting transcriptional repression.[1,2] Human HDACs are divided into five classes/subclasses on the basis of their homology to yeast HDACs: class I (HDAC1, 2, 3, and 8), class IIa (HDAC4, 5, 7, and 9), class IIb (HDAC6 and 10), class III (SIRT1, 2, 3, 4, 5, 6, and 7), and class IV (HDAC11). Because aberrant epigenetic changes are hallmarks of cancer, HDACs are promising targets for the development of anticancer drugs. Inhibitors of HDACs can induce cell-cycle arrest, differentiation, and tumor cell death. In fact, several HDAC inhibitors are currently in clinical trials for the treatment of both solid and hematologic malignancies.[1,2]

In our search for HDAC inhibitors, we isolated a novel trichostatin analogue, JBIR-17, in which a serine residue is attached to C-1 of trichostatic acid via an amide bond, from the culture of *Streptomyces* sp. 26634.[3] Upon further screening, we discovered three additional trichostatin analogues, JBIR-109 (**1**), JBIR-110 (**2**), and JBIR-111 (**3**), from the culture of *Streptomyces* sp. RM72, which was associated with a marine sponge collected from a mesopelagic area. We report herein the isolation, structure elucidation, and biological activities of **1**−**3**.

Streptomyces sp. RM72 was cultured in production medium with 50% artificial seawater. Compounds **1**−**3**, together with trichostatin A (**4**)[4] and trichostatic acid (**5**),[5] were recovered from the culture supernatant by using HP-20 resin, followed by purification with sequential chromatography utilizing MPLC and HPLC.

The structures of **1**−**3** were primarily elucidated by spectroscopic analyses. The presence of an amide functional group was suggested by an IR absorption at 1650 cm^{-1}. The UV absorption maxima at 340 and 264 nm, together with ^{1}H and ^{13}C NMR data for **1**−**3** (Table 1 and Table S1), suggested that the basic structural skeletons were identical to that of **5**. Detailed structural information was obtained from the HSQC, HMBC, and DQF-COSY spectra of **1**−**3** (Figure 1).

The molecular formula of **1** was established as $C_{22}H_{28}N_2O_6$ on the basis of HRESIMS data ($[M + H]^+$; *m/z*, 417.2029). In addition to the trichostatic acid portion of the structure, the sequence from the α-methine proton H-2′ (δ_H 4.50; δ_C 53.5) to methylene protons H-4′ (δ_H 2.40) through methylene protons H-3′ (δ_H 1.98, 2.20) was observed. HMBC correlations between H-3′ and two carboxylic carbonyl carbons, C-1′ (δ_C 175.3) and C-5′ (δ_C 176.5), suggested a glutamic acid moiety. Finally, HMBC correlations between both the olefinic proton H-2 and the α-methine proton H-2′ and an amide carbonyl carbon C-1 (δ_C 169.0) established the structure of **1** as a glutamate-substituted trichostatic acid.

The molecular formulas of **2** and **3** were determined to be $C_{19}H_{26}N_2O_5S$ and $C_{21}H_{28}N_2O_5$ on the basis of the HRESIMS data ($[M + H]^+$, *m/z* 395.1655 and $[M + H]^+$, *m/z* 389.2067), respectively. The trichostatic acid core structure in **2** and **3** was established on the basis of NMR data similarly to that described for **1**. For **2**, a COSY correlation between the amino methylene protons H-1′ (δ_H 3.67, δ_C 36.7) and methylene protons H-2′

Received: October 17, 2011
Published: January 25, 2012

Chart 1

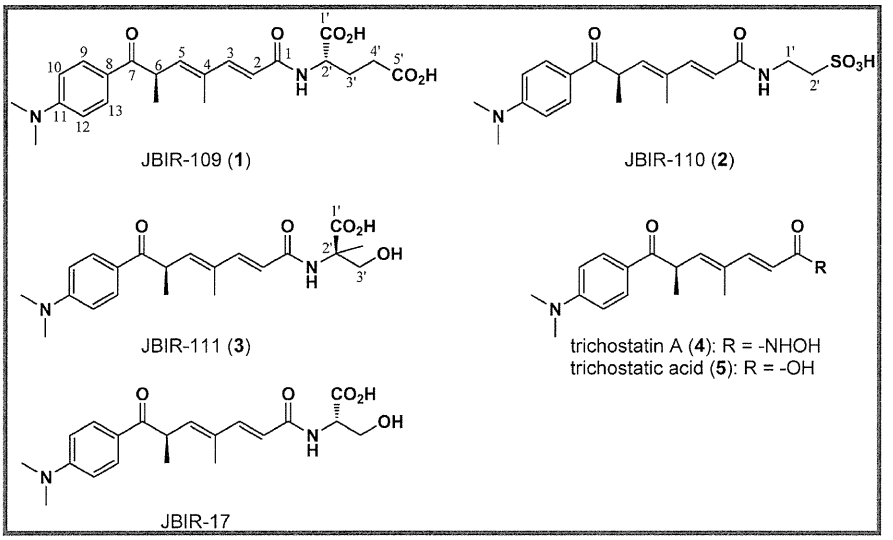

Table 1. ^{1}H (600 MHz) and ^{13}C (150 MHz) NMR Spectroscopic Data for JBIR-109 (1) in CD_3OD

position	δ_C, type	δ_H (J in Hz)
1	169.0, C	
2	120.3, CH	6.09, d (15.5)
3	146.6, CH	7.16, d (15.5)
4	134.5, C	
5	141.5, CH	5.91, d (9.5)
6	41.8, CH	4.53, dq (6.5, 9.5)
7	201.5, C	
8	124.8, C	
9, 13	132.0, CH	7.86, d (9.0)
10, 12	112.0, CH	6.73, d (9.0)
11	155.5, C	
4-methyl	12.8, CH_3	1.95, s
6-methyl	18.3, CH_3	1.27, d (6.5)
11-*N*,*N*-dimethyl	40.1, CH_3	3.06, s
Glu		
1′	175.3, C	
2′	53.5, CH	4.50, dd (6.0, 9.0)
3′	28.3, CH_2	2.20, m
		1.98, m
4′	31.4, CH_2	2.40, m
5′	176.5, C	

(δ_H 2.99), together with an HMBC correlation from H-1′ to amide carbonyl carbon C-1 (δ_C 168.7), revealed that an additional two-carbon fragment was present at the carboxy terminus of the trichostatic acid skeleton. The NMR spectra of the amino acid moiety [C-1′ (δ_H 3.67, δ_C 36.7) and C-2′ (δ_H 2.99, δ_C 51.4)] in **2** were similar to those of taurine [C-1′ (δ_H 3.55, δ_C 36.8) and C-2′ (δ_H 2.95, δ_C 51.5)] in the literature.[6] Finally, a sulfonic acid residue, the presence of which was deduced from the molecular formula, was attached to H-2′, establishing that **2** was a trichostatic acid analogue modified with taurine as shown in Figure 1.

The NMR spectroscopic data for **3** closely resembled those of JBIR-17. An HMBC correlation from the singlet methyl protons 3′-Me (δ_H 1.48) to carboxy carbonyl carbon C-1′ (δ_C 177.1), quaternary carbon C-2′ (δ_C 62.4), and a hydroxymethyl carbon (δ_C 66.0) suggested the presence of an α-methylserine moiety. The molecular formula of **3** indicated a C-2′-methylated congener of JBIR-17. In addition, the connectivity of trichostatic acid and the α-methylserine moiety was confirmed by NMR experiments in DMSO-d_6. HMBC correlations between the amide proton (δ_H 7.85) and C-1 (δ_C 164.6), C-1′ (δ_C 174.8), C-2′ (δ_C 60.0), C-3′ (δ_C 65.2), and 1′-methyl (δ_C 20.1) indicated that the α-methylserine connects to C-1 of trichostatic acid through an amide bond.

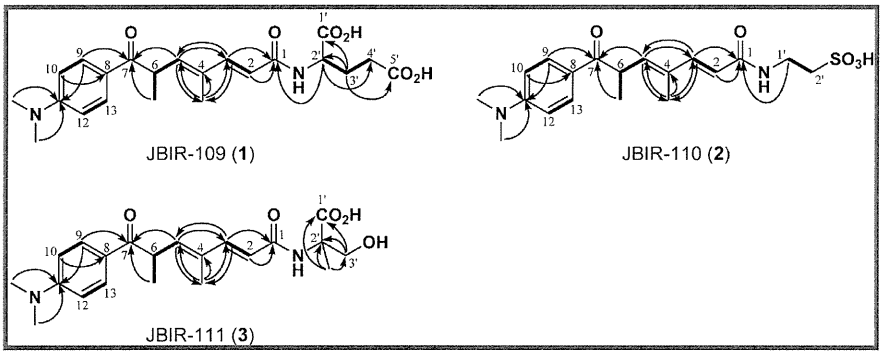

Figure 1. Key correlations observed in 2D NMR spectra of **1**, **2**, and **3**. Bold lines show ^{1}H–^{1}H DQF-COSY correlations, and arrows show HMBC results.

dx.doi.org/10.1021/np200843k | *J. Nat. Prod.* 2012, 75, 285–289

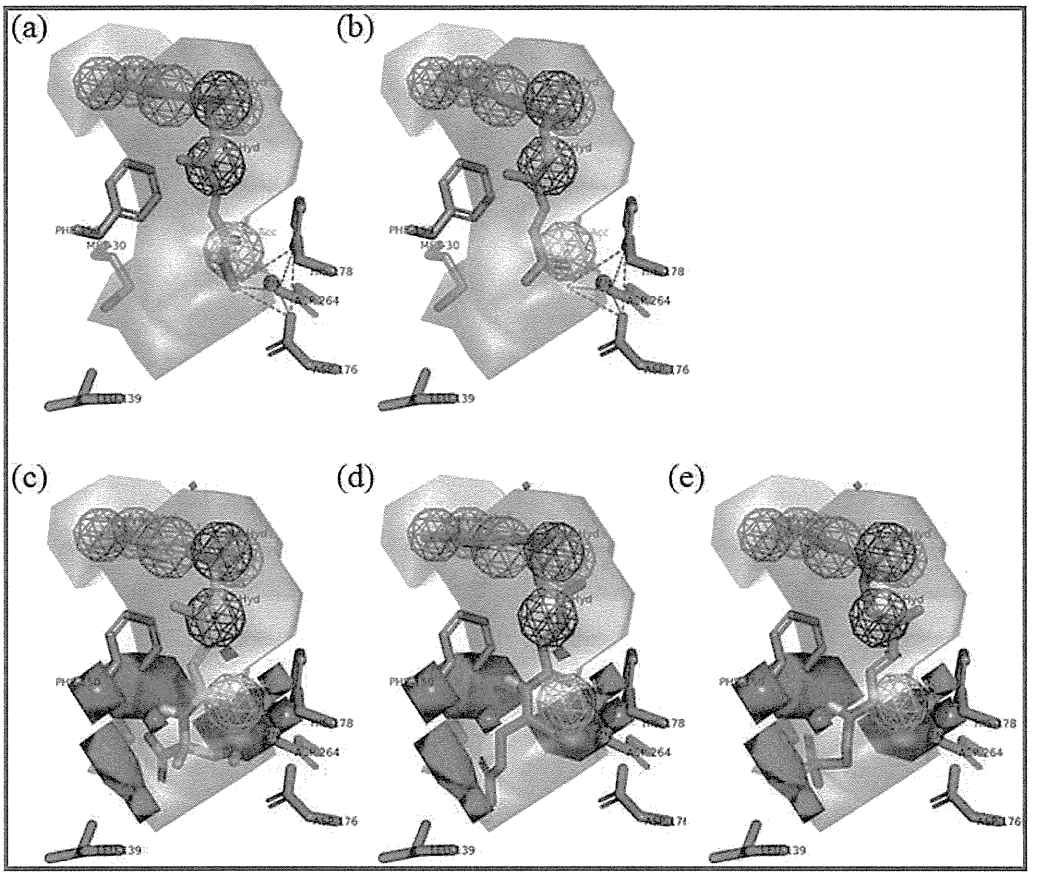

Figure 2. Proposed binding models for **4** (a), **5** (b), **1** (c), **2** (d), and **3** (e) to human HDAC1. Carbon atoms of **1** (purple, blue), **2** (orange), and **3** (cyan) are shown. Consensus features of the pharmacophore models are generated for the five molecules: hydrogen bond acceptor (cyan feature), aromatic ring region (green feature), and hydrophobic region (dark green feature). The shape of the overall volume for the five molecules is defined by the transparent surface. HDAC1 residues around the compounds are shown in stick (gray) representation. Tetrahedral zinc complexes in the protein cavity, which are composed of a nitrogen atom of a histidine residue, two carbonyl groups of aspartic acid residues, and the carbonyl group of the compounds, are represented by the polyhedral cage with purple dashed lines in (a) and (b). Red and blue in (c, d, e) show negative and positive regions, respectively, predicted by electrostatic analysis using 3D-QSAR.

The absolute configurations of the glutamic acid residue in **1** and the α-methylserine residue in **3** were defined by Marfey's method.[7] Comparisons of retention times between the FDAA-treated residues from the hydrolysates of standards established the configurations of the glutamic acid residue in **1** as L and the α-methylserine residue in **3** as *R*. It is intriguing to note that the configuration of the serine in **3** is opposite that of the serine in JBIR-17 isolated from another *Streptomyces* sp.[3] Because the specific rotation value ($[\alpha]^{25}_{D}$ +29, *c* 0.10, MeOH) of **4** isolated with **1**–**3** is of the same sign and similar to the value ($[\alpha]^{25}_{D}$ +63 (*c* 0.10, MeOH)[4]) reported for **4**, the absolute configurations of the trichostatic acid residues of **1**–**3** are proposed to be the same as for (*R*)-trichostatin A.[4]

To evaluate the HDAC inhibitory activity of **1**–**5**, we employed HDAC1 as a representative HDAC. The IC_{50} values against HDAC1 of **1**–**5** were 48, 74, 57, 0.012, and 73 μM, respectively. The inhibitory activities of **1**–**3** and **5** against HDAC1 were >1000 times weaker than that of **4**. These results are consistent with the reported model for HDAC1 inhibition by trichostatin A, in which the hydroxamate functionality is essential to exert the activity.[8] In addition, we performed computational binding analyses using the 3D-quantitative structure–activity relationship (QSAR) for **1**–**5** (Figure 2). The results show that the main reason for the low binding affinity of **5** to HDAC1 can be ascribed to the inability to form a stable tetrahedral zinc complex in the protein cavity. Meanwhile, the electrostatic analysis by 3D-QSAR showed that the low-binding affinity of **1**–**3** is due to an unfavorable interaction between the hydrophobic surface consisting of Leu-139, Phe-150, and Met-30 within the protein cavity and the polar functional groups in these compounds.

HDAC inhibitors are promising antitumor agents and also play important roles as low-molecular probes to study epigenetics. These results provide valuable information for developing new HDAC inhibitors.

EXPERIMENTAL SECTION

General Experimental Procedures. Optical rotations were measured using a Horiba SEPA-300 polarimeter. UV and IR spectra were measured with a Beckman Coulter DU730 UV/vis spectrophotometer and a Horiba FT-720 spectrophotometer, respectively. NMR spectra were collected in CD_3OD using a Varian NMR System 600 NB CL spectrometer with the residual solvent peaks referenced to δ_C 49.15 and δ_H 3.31 ppm. The optimizations of HMBC and HSQC spectra for appropriate couplings were 8 and 140 Hz, respectively. HRESIMS data were recorded using a Waters LCT-Premier XE mass spectrometer. Reversed-phase MPLC was conducted on a Purif-Pack ODS-100 column (Shoko Scientific). Analytical reversed-phase HPLC was conducted using an XBridge C18 column (4.6 i.d. × 150 mm;

dx.doi.org/10.1021/np200843k | *J. Nat. Prod.* 2012, 75, 285–289

Waters) in conjunction with a Waters 2996 photodiode array detector and a Waters 3100 mass detector. Analytical reversed-phase UPLC (Waters) was performed using a BEH ODS column (2.1 i.d. × 50 mm; Waters) in conjunction with a Waters ACQUITY UPLC photodiode array eλ detector and an LCT-Premier XE mass spectrometer. Preparative reversed-phase HPLC was conducted using an XBridge Prep C18 column (20 i.d. × 150 mm) in conjunction with a Hitachi High Technologies L-2455 photodiode array detector.

Biological Material. *Streptomyces* strain RM72 was isolated from an unidentified marine sponge collected at a depth of 195 m at the position 28° 53′ 35.8″ N, 129° 29′ 57.0″ E near Takara Island, Kagoshima Prefecture, Japan. To identify the strain, a partial 16S rRNA gene sequence was determined (DDBJ accession number AB683042), and comparison with sequences in the Eztaxon type strain database[9] revealed that the closest phylogenetic neighbor of the strain was *Streptomyces angustmycinicus* NBRC 3934^T (AB184817), with a sequence identity of 100%.

Fermentation. The strain was cultivated in 50 mL test tubes each containing 15 mL of the seed medium consisting of 1.0% starch (Kosokagaku), 1.0% Polypepton (Nihon Pharmaceutical), 1.0% molasses (Dai-Nippon Meiji Sugar), and 1.0% meat extract (Extract Ehlrich, Wako Pure Chemical Industry) (pH 7.2). The test tubes were shaken on a reciprocal shaker (320 rpm) at 27 °C for 2 days. Aliquots (2.5 mL) of the broth were then transferred to 500 mL baffled Erlenmeyer flasks containing 100 mL of the production medium consisting of 1.0% starch, 1.0% glucose (Kanto Chemical), 1.0% glycerin (Nacalai Tesque), 0.5% Polypepton, 0.2% yeast extract (BD Biosciences), 1.0% corn-steep liquor (Oriental Yeast), 0.1% NaCl (Kanto Chemical), and 0.32% $CaCO_3$ (Kozaki Pharmaceutical) in 50% artificial seawater (Marine art SF-1, Tomita Pharmaceutical) (pH 7.4 before sterilization) and cultured on a rotary shaker (180 rpm) at 27 °C for 5 days.

Isolation. The fermentation broth (2 L) was separated into the mycelial cake and supernatant by centrifugation. The supernatant was subsequently applied to a Diaion HP-20 column, and the column was then washed with H_2O and eluted with 100% MeOH. After evaporation of the 100% MeOH eluent *in vacuo*, the resulting residue was subjected to reversed-phase MPLC by using an aqueous MeOH linear gradient system (20–100% MeOH). The 20–30% MeOH eluate (145 mg) was then subjected to preparative reversed-phase HPLC with 55% aqueous MeOH containing 0.1% formic acid (flow rate, 6 mL/min) to give JBIR-109 (**1**, t_R = 13.7 min, 3.5 mg) and JBIR-110 (**2**, t_R = 11.3 min, 3.4 mg). In addition, the 30–40% MeOH eluate (107 mg) was purified by preparative reversed-phase HPLC using 58% aqueous MeOH containing 0.1% formic acid (flow rate, 6 mL/min) to give JBIR-111 (**3**, t_R = 13.7 min, 3.5 mg), trichostatin A (**4**, t_R = 11.3 min, 0.7 mg), and trichostatic acid (**5**, t_R = 13.0 min, 1.0 mg).

JBIR-109 (1): colorless, amorphous solid; $[\alpha]^{25}_D$ −27 (*c* 0.10, MeOH); UV (MeOH) λ_{max} (log ε) 340 (4.2), 265 (4.2) nm; IR (KBr) ν_{max} 1660 cm^{-1}; ^{1}H NMR (600 MHz, CD_3OD) and ^{13}C NMR (150 MHz, CD_3OD), see Table 1; HRESIMS *m/z* 417.2029 [M + H]$^+$ (calcd for $C_{22}H_{29}N_2O_6$, 417.2026).

JBIR-110 (2): colorless, amorphous solid; $[\alpha]^{25}_D$ +12 (*c* 0.10, MeOH); UV (MeOH) λ_{max} (log ε) 340 (4.2), 264 (4.2) nm; IR (KBr) ν_{max} 1660 cm^{-1}; ^{1}H NMR (600 MHz, CD_3OD) and ^{13}C NMR (150 MHz, CD_3OD), see Table 2; HRESIMS *m/z* 395.1655 [M + H]$^+$ (calcd for $C_{19}H_{27}N_2O_5S$, 395.1641).

JBIR-111 (3): colorless, amorphous solid; $[\alpha]^{25}_D$ +33 (*c* 0.10, MeOH); UV (MeOH) λ_{max} (log ε) 340 (4.1), 265 (4.2) nm; IR (KBr) ν_{max} 1650 cm^{-1}; ^{1}H NMR (600 MHz, CD_3OD) and ^{13}C NMR (150 MHz, CD_3OD), see Table 2; HRESIMS *m/z* 389.2067 [M + H]$^+$ (calcd for $C_{21}H_{29}N_2O_5$, 389.2076).

Determination of Amino Acid Configurations. A sample of **1** or **3** (1.0 mg) was hydrolyzed in 6 N HCl (0.2 mL) at 110 °C for 12 h. After acid hydrolysis, the reaction solution was adjusted to neutral pH and evaporated *in vacuo*. The residue was dissolved in 10 mL of EtOAc–H_2O (1:1). The amino acid mixture was then recovered in the aqueous layer. After drying the aqueous layer *in vacuo*, it was dissolved in 5% $NaHCO_3$ (600 μL), and FDAA (Marfey's reagent, 0.2 mg) in acetone (600 μL) was added. The mixture was then heated in an oil bath at 70 °C for 10 min with frequent shaking. The reaction products were analyzed by the UPLC system. A Waters BEH ODS column was developed with 20% aqueous MeCN containing 0.1% formic acid at a flow rate of 0.3 mL/min. The retention times of the FDAA derivatives were determined by monitoring UV absorption at 340 nm and the positive mode of ESIMS. The retention times of the standard FDAA derivatives were as follows: L-Glu, 2.34 min; D-Glu, 2.95 min; α-methyl-*R*-Ser, 2.10 min; and α-methyl-*S*-Ser, 2.74 min. The retention times of the FDAA derivatives from **1** and **3** were 2.38 min for Glu and 2.10 for α-methyl-Ser, respectively.

Table 2. ^{1}H (600 MHz) and ^{13}C (150 MHz) NMR Spectroscopic Data for Amino Acid Moieties of JBIR-110 (2) and JBIR-111 (3) in CD_3OD

JBIR-110 (2)			JBIR-111 (3)		
position	δ_C, type	δ_H (*J* in Hz)	position	δ_C, type	δ_H (*J* in Hz)
Taurine			MeSer		
1′	36.7, CH_2	3.67, t (6.6)	1′	177.1, C	
2′	51.4, CH_2	2.99, t (6.6)	2′	62.4, C	
			3′	66.0, CH_2	3.90, brd (11.0)
					3.85, brd (11.0)
			3′-methyl	20.8, CH_3	1.48, s

HDAC1 Inhibitory Assay. The human HDAC1 inhibitory activity was evaluated using the HDAC1 inhibitor screening assay kit (Cayman Chemical) according to the manufacturer's protocol. Briefly, 140 μL of assay buffer, 10 μL of diluted HDAC1, and 10 μL of samples were added in a 96-well black plate. To initiate the reaction, 10 μL of the HDAC substrate (final concentration, 200 μM) was added. After incubation for 30 min at 37 °C, 40 μL of the developer was added and mixed. After further incubation for 15 min at room temperature, the fluorescence (excitation, 340 nm; emission, 450 nm) was measured. Trichostatin A was used as a positive control (IC_{50} = 12 nM).

Quantitative Structure–Activity Relationship. 3D-QSAR analysis for compounds **1**–**5** was carried out using the homology model of HDAC1 and the docking simulation. A three-dimensional structure of human HDAC1 was constructed by a homology modeling approach with the structural template of the crystal structure of an HDAC homologue complexed with trichostatin A (PDB-ID: 1C3R),[10] incorporated in the program Prime with default parameters (Schrödinger, LLC). The sequence identity between HDAC1 and the HDAC homologue protein was 32% (see Supporting Information, Figure 24S). The structural template was selected by using a similarity measure from the sequence-structure alignment and in addition from the protein–ligand interactions in the active-site environment obtained by induced fit modeling. To prepare the compounds with active conformations for 3D-QSAR analysis, molecular models of the compound-bound HDAC1 were generated by docking simulation using Glide SP mode with default parameters (Schrödinger, LLC). The grid center for docking was defined using the reference position of trichostatin A on 1C3R, which is the structural template used in the homology modeling step. 3D-QSAR analysis with the aligned active conformation from docking results was performed using the Auto-GPA protocol on MOE (Chemical Computing Group). The visualizations were generated by PyMOL (Schrödinger, LLC).

■ ASSOCIATED CONTENT

Supporting Information

^{1}H and ^{13}C NMR, DQF-COSY, HSQC, CT-HMBC, and HRESIMS spectra of **1**–**3** are available free of charge via the Internet at http://pubs.acs.org.

AUTHOR INFORMATION

Corresponding Author

*(M.T.) Tel: +81-3-3599-8305. Fax: +81-3-3599-8494. E-mail: motoki-takagi@aist.go.jp. (K.S.) Tel: +81-3-3599-8305. Fax: +81-3-3599-8494. E-mail: k-shinya@aist.go.jp.

ACKNOWLEDGMENTS

This work was supported by a grant from the New Energy and Industrial Technology Department Organization (NEDO). The sponge was collected during the NT-09-17 cruise of Natsushima, by the Japan Agency for Marine-Earth Science and Technology (JAMSTEC).

REFERENCES

(1) Carew, J. S.; Giles, F. J.; Nawrocki, S. T. *Cancer Lett.* **2008**, *269*, 7−17.

(2) Shankar, S.; Srivastava, R. K. *Adv. Exp. Med. Biol.* **2008**, *615*, 261−298.

(3) Ueda, J.; Hwang, J. H.; Maeda, S.; Kato, T.; Ochiai, A.; Isshiki, K.; Yoshida, M.; Takagi, M.; Shin-ya, K. *J. Antibiot.* **2009**, *62*, 283−285.

(4) Morikawa, H.; Ishihara, M.; Takezawa, M.; Hirayama, K.; Suzuki, E.; Komoda, Y.; Shibai, H. *Agric. Biol. Chem.* **1985**, *49*, 1365−1370.

(5) Tsuji, N.; Kobayashi, M.; Nagashima, K.; Wakisaka, Y.; Koizumi, K. *J. Antibiot.* **1976**, *29*, 1−6.

(6) Bi, D.; Chai, X.-Y.; Song, Y.-L.; Lei, Y.; Tu, P.-F. *Chem. Pharm. Bull.* **2009**, *57*, 528−531.

(7) Marfey, P. *Carlsberg Res. Commun.* **1984**, *49*, 591−596.

(8) Yoshida, M.; Kijima, M.; Akita, M.; Beppu, T. *J. Biol. Chem.* **1990**, *265*, 17174−17179.

(9) Chun, J.; Lee, J. H.; Jung, Y.; Kim, M.; Kim, S.; Kim, B. K.; Lim, Y. W. *Int. J. Syst. Evol. Microbiol.* **2007**, *57*, 2259−2261.

(10) Finnin, M. S.; Donigian, J. R.; Cohen, A.; Richon, V. M.; Rifkind, R. A.; Marks, P. A.; Breslow, R.; Pavletich, N. P. *Nature* **1999**, *401*, 188−193.

Organic & Biomolecular Chemistry

Cite this: *Org. Biomol. Chem.*, 2012, **10**, 736

www.rsc.org/obc

PAPER

Cyclopropane-based stereochemical diversity-oriented conformational restriction strategy: Histamine H_3 and/or H_4 receptor ligands with the 2,3-methanobutane backbone

Mizuki Watanabe,[a] Takaaki Kobayashi,[a] Takatsugu Hirokawa,[b] Akira Yoshida,[c] Yoshihiko Ito,[c] Shizuo Yamada,[c] Naoki Orimoto,[d] Yasundo Yamasaki,[d] Mitsuhiro Arisawa[a] and Satoshi Shuto*[a]

Received 1st September 2011, Accepted 11th October 2011
DOI: 10.1039/c1ob06496g

The stereochemical diversity-oriented conformational restriction strategy can be an efficient method for developing specific ligands for drug target proteins. To develop potent histamine H_3 and/or H_4 receptor ligands, a series of conformationally restricted analogs of histamine with a chiral *trans*- or *cis*-4-amino-2,3-methano-1-(1*H*-imidazol-4-yl)butane structure was designed based on this strategy. These stereochemically diverse compounds were synthesized from previously developed versatile chiral cyclopropane units. Among these analogs, a *trans*-cyclopropane-type compound, (2*S*,3*R*)-4-(4-chlorobenzylamino)-2,3-methano-1-(1*H*-imidazol-4-yl)butane (**5b**), has remarkable antagonistic activity to both the H_3 (K_i = 4.4 nM) and H_4 (K_i = 5.5 nM) receptors, and a *cis*-cyclopropane-type compound, (2*R*,3*R*)-4-amino-2,3-methano-1-(1*H*-imidazol-4-yl)butane (**6a**), is a potent and selective H_3 receptor partial agonist (K_i = 5.4 nM). Although (2*S*,3*R*)-4-amino-2,3-methano-1-(1*H*-imidazol-4-yl)butane (**5a**) does not have a hydrophobic group which the usual H_3 receptor antagonists have, it was found to be a potent H_3 receptor antagonist (K_i = 20.1 nM). Thus, a variety of compounds with different pharmacological properties depending on the cyclopropane backbones and also on the side-chain functional groups were identified. In addition to the previously used 1,2-methanobutane backbone, the 2,3-methanobutane backbone also worked effectively as a cyclopropane-based conformational restriction structure. Therefore, the combination of these two cyclopropane backbones increases the stereochemical and three-dimensional diversity of compounds in this strategy, which can provide a variety of useful compounds with different pharmacological properties.

Introduction

The histamine H_3 receptor, a member of the G_i protein-coupled receptors (GPCRs) distributed mainly in the central nervous system, is of interest as a potential drug target.[1] Agonists and antagonists to the H_3 receptor are considered to be potential drugs for the treatment of sleep disorders, migraines, asthma, inflammation, or ulcers,[2a] and for the treatment of Alzheimer's disease, attention-deficit/hyperactivity disorder (ADHD), schizophrenia, depression, dementia, or epilepsy,[2b] respectively.

On the other hand, the histamine H_4 receptor, also one of the GPCRs, is expressed in immunocytes, such as eosinophils or mast cells, and chemotaxis of these cells *via* histamine is triggered through H_4 receptor activation.[3a] Accordingly, H_4 receptor antagonists may be effectively used in new therapeutic modalities for the treatment of allergic diseases.[3b,c]

Although GPCRs, including the H_3 and H_4 receptors, are important targets for drug development,[4] structural analysis of GPCRs is difficult due to the membranous nature of these proteins and to their very low natural abundance, compared with that of proteins soluble in blood or cytosol.[5] Therefore, structural data on the drug target GPCRs are generally poor, and a method for effectively identifying compounds that target GPCRs without any structural data is required in drug development. Thus, we previously reported a stereochemical diversity-oriented conformational restriction strategy to develop compounds that bind selectively to structure-unknown target proteins such as GPCRs.[6,7] To realize the strategy, we devised versatile chiral cyclopropane units with different stereochemistries,[6a,c] shown in Fig. 1, and, by using these units, a series of cyclopropane-based conformationally restricted analogs[8] with

[a]*Faculty of Pharmaceutical Sciences, Hokkaido University, Kita-ku, Sapporo, 060-0812, Japan. E-mail: shu@pharm.hokudai.ac.jp*
[b]*Computational Biology Research Center, National Institute of Advanced Industrial Science and Technology, Aomi, Koutou-ku, Tokyo, 135-0064, Japan*
[c]*Department of Pharmacokinetics and Pharmacodynamics and Global Center of Excellence (COE), School of Pharmaceutical Sciences, University of Shizuoka, 52-1 Yada, Suruga-ku, Shizuoka, 422-8526, Japan*
[d]*Hanno Research Center, Taiho Pharmaceutical Co. Ltd., Misugidai, Hanno, 357-8527, Japan*

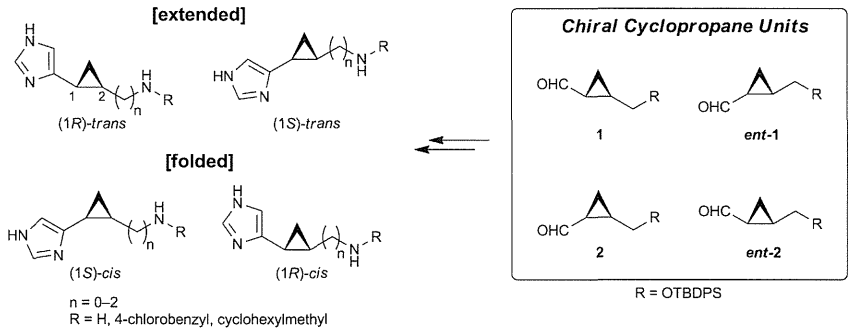

Fig. 1 Conformationally restricted analogs of histamine having the 1,2-methanoalkylimidazole backbone prepared from chiral cyclopropane units.

stereochemical diversity can be designed and synthesized effectively.

Based on the strategy, we actually designed a series of conformationally restricted analogs of histamine with different stereochemistries, which were synthesized from the chiral cyclopropane units (Fig. 1).[6] In these conformationally restricted analogs having an aminoalkyl-1,2-methanoimidazole backbone, the imidazole and the amino side-chain moieties are located in a variety of spatial arrangements due to the conformationally restricted 1,2-methanoalkyl backbone. Consequently, a series of these analogs is not only stereochemically diverse but also three-dimensionally diverse as a molecule. Some of these analogs shown in Fig. 2 were identified as potent histamine receptor ligands; *e.g.*, AEIC (**3**) with a (1*S*)-*cis*-cyclopropane structure is the first highly selective H_3 receptor agonist,[6b] and (1*R*,2*S*)-2-[2-(4-chlorobenzylamino)ethyl]-1-(1*H*-imidazol-4-yl)cyclopropane [(*R*)-CEIC (**4**)] with a (1*R*)-*trans*-cyclopropane structure and its enantiomer (*S*)-CEIC (***ent*-4**) with a (1*S*)-*trans*-cyclopropane structure were highly potent antagonists to both the H_3 receptor and the H_4 receptor.[6c]

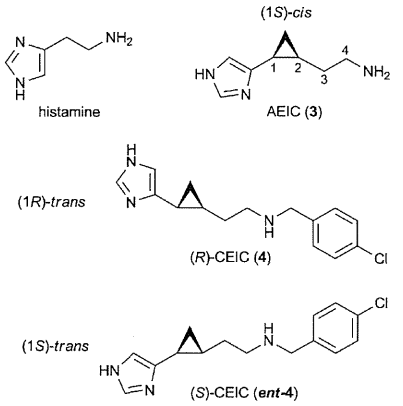

Fig. 2 Histamine and its conformationally restricted analogs having the 1,2-methanobutylimidazole backbone.

In the course of our studies to develop further potent H_3 and H_4 receptor ligands, we newly designed a series of conformationally restricted analogs of histamine based on the stereochemical diversity-oriented strategy, namely **5a,b** and **6a,b**, and their enantiomers, ***ent*-5a,b** and ***ent*-6a,b**, all having a 2,3-methanobutylimidazole structure (Fig. 3). In this report, we

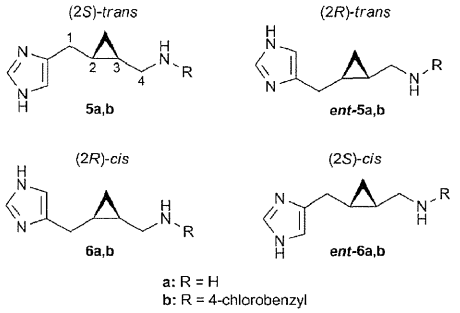

Fig. 3 Conformationally restricted analogs of histamine having the 2,3-methanobutylimidazole backbone.

describe the design, synthesis, and pharmacological effects of these compounds.

Results and discussion

Design of compounds

Our previous studies demonstrated that conformational restriction of histamine by the 4-amino-1,2-methanobutane backbone was effective for the H_3 and/or H_4 receptor binding, where the folded *cis*-cyclopropane structure like AEIC (**3**) and the extended *trans*-cyclopropane structure like (*R*)- and (*S*)-CEIC (**4** and ***ent*-4**) are suitable for the binding as an agonist and an antagonist, respectively.[6b,c] They also showed that functional conversion of an agonist into an antagonist could occur by introducing a hydrophobic group, such as a chlorobenzyl group,[2b] at the terminal primary amino moiety of the 4-amino-1,2-methanobutane backbone.[6c] Considering these results, we designed the regioisomeric derivatives of AEIC (**3**) and (*R*)- and (*S*)-CEIC (**4** and ***ent*-4**), which have a 4-amino-2,3-methanobutane backbone, as shown in Fig. 3, for identifying new H_3 and/or H_4 receptor ligands. In these compounds, the folded *cis*-cyclopropane or the extended *trans*-cyclopropane structure on the four carbon (butane) backbone is preserved, and accordingly, the imidazole and the basic nitrogen moieties, which are key components in these structures for binding to the histamine receptors, might be located in space similarly to those of the previously identified potent analogs having the 4-amino-1,2-methanobutane backbone. Also, the regioisomeric 2,3-methano structure could change spatial arrangement and flexibility around the imidazole and the basic

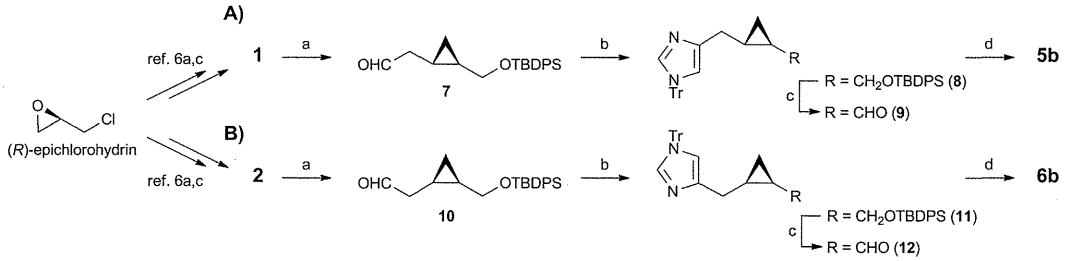

Scheme 1 *Conditions*: a) 1) $MeOCH_2PPh_3Cl$, $NaN(TMS)_2$, THF, 0 °C, 2) HCl, aq. acetone, 0 °C, 85% (**7**), 92% (**10**); b) 1) $TosCH_2NC$, NaCN, EtOH, 0 °C, 2) sat. NH_3 in EtOH, steel tube, 120 °C, 3) TrCl, pyridine, 48% (**8**), 51% (**11**); c) 1) TBAF, THF, 2) Dess–Martin periodinane, CH_2Cl_2, 78% (**9**), 65% (**12**); d) 1) 4-chlorobenzylamine, 2-picoline borane, AcOH, MeOH, 2) TrCl, Et_3N, CH_2Cl_2, 3) HCl, aq. EtOH, 78 °C, 30% (**5b**), 49% (**6b**).

nitrogen moieties, compared with those in the 1,2-methano lead compounds AEIC (**3**) and (*R*)- and (*S*)-CEIC (**4** and ***ent*-4**), which would affect the biological activity. We hoped to develop both agonists and antagonists, and therefore, compounds with a free primary amino function (**a**-series, as agonists) and compounds with a 4-chlorobenzylamino function (**b**-series, as antagonists) were designed for synthesis.

Thus, we expected that the 2,3-methanobutane backbone might be useful as an alternative conformationally restricted structure in the cyclopropane-based stereochemical diversity-oriented strategy.

Chemistry

Although much effort has been devoted to developing practical methods for preparing chiral cyclopropanes, synthesizing cyclopropane derivatives with a desired stereochemistry is often troublesome.[9] We devised the chiral units (Fig. 1), which are composed of four stereoisomeric cyclopropane derivatives bearing two adjacent carbon substituents in a *trans* or *cis* relationship, namely **1** and **2**, and their enantiomers, ***ent*-1** and ***ent*-2**, for cyclopropane-based conformational restriction.[6a] These units, which are generally useful for synthesizing various compounds having an asymmetric *trans*- or *cis*-cyclopropane structure,[6] were employed as the key intermediates in this study.

The synthesis of the *trans*-cyclopropane compound **5b** and the *cis*-cyclopropane compound **6b** with a 4-chlorobenzyl group (**b**-series) from the chiral cyclopropane unit **1** and **2**, respectively, is shown in Scheme 1. These units **1** and **2** were prepared from (*R*)-epichlorohydrin according to the method reported previously.[6a,c] The Wittig reaction of the unit **1** with $MeOCH_2PPh_3Cl/NaN(TMS)_2$, followed by acidic treatment gave the one carbon-elongated aldehyde **7**. The imidazole ring was constructed by treating **7** with tosylmethyl isocyanide and NaCN followed by heating in NH_3/EtOH.[10] The resulting imidazole product without purification was further treated with TrCl in pyridine to give the *N*-tritylimidazolylmethylcyclopropane derivative **8** in 48% overall yield. After removal of the silyl-protecting group of **8**, the resulting cyclopropanemethanol was oxidized to afford the aldehyde **9**. Introduction of a 4-chlorobenzylamino function at the terminal carbon was next investigated under reductive amination conditions. Thus, treatment of the aldehyde **9** with 4-chlorobenzylamine and 2-picoline borane in AcOH/MeOH, and subsequent acidic removal of the trityl group of the product gave the desired *trans*-cyclopropane-type target compound **5b** (Scheme 1A). By a similar procedure, the *cis*-cyclopropane-type target compound **6b** was synthesized from the *cis*-cyclopropane unit **2** (Scheme 1B). The enantiomers, ***ent*-5b** and ***ent*-6b**, were also synthesized from ***ent*-1** and ***ent*-2**, respectively.

The synthesis of **5a** and **6a** with a terminal primary amine (**a**-series) is shown in Scheme 2. Treatment of the aldehyde **9** with *t*-BuS(O)NH_2 and $CuSO_4$ in CH_2Cl_2 gave the corresponding sulfinylimine product, which was, without purification, reduced with $NaBH_4$/MeOH to afford the sulfinylamide **13**. Simultaneous removal of the trityl and sulfinyl groups by treating **13** with HCl in EtOH produced the target *trans*-cyclopropane-type compound **5a** (Scheme 2A). Similarly, the *cis*-cyclopropane-type compound **6a** was prepared from the *cis*-cyclopropane aldehyde **12** (Scheme 2B). The corresponding enantiomers, ***ent*-5a** and ***ent*-6a**, were also synthesized from the *trans*- and *cis*-cyclopropane aldehydes, ***ent*-9** and ***ent*-12**, respectively.

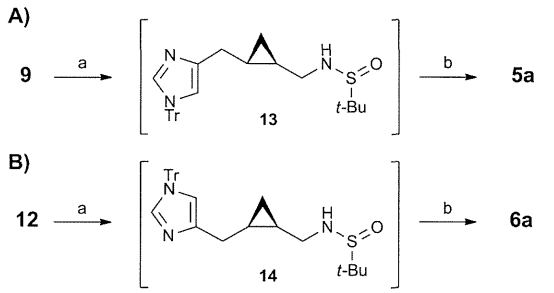

Scheme 2 *Conditions*: a) 1) *t*-BuS(O)NH_2, $CuSO_4$, CH_2Cl_2, 2) $NaBH_4$, MeOH, 0 °C; b) HCl, EtOH, 78 °C, 50% from **9** (**5a**), 59% from **12** (**6a**).

Pharmacological effects

The binding affinities of the conformationally restricted analogs with the 2,3-methanobutane backbone for the human H_3 receptor subtype using [^{3}H]N^α-methylhistamine and also for the human H_4 receptor subtype using [^{3}H]histamine were investigated, according to the previously reported procedure.[6c]

The binding affinities of the compounds for the H_3 receptor are summarized in Table 1. All of the synthesized compounds inhibited the specific binding of [^{3}H]N^α-methylhistamine to the H_3 receptor in a concentration-dependent manner. Of these compounds, all the *trans*-analogs, **5a**, ***ent*-5a**, **5b**, and ***ent*-5b**, had

Table 1 Effects of compounds on the human H_3 and H_4 receptor subtypes[a]

Compound	Structure	H_3			H_4			Selectivity
		K_i (nM)	act.[b] (%)	inh.[c] (%)	K_i (nM)	act.[b] (%)	inh.[c] (%)	$K_i(H_3)/K_i(H_4)$
5a	2,3-M[d]/(2*S*)-*trans*	20.1 ± 5.1	2.5	94	119 ± 25	11	45	0.17
***ent*-5a**	2,3-M/(2*R*)-*trans*	9.3 ± 0.8	17	72	50.9 ± 11	30	40	0.18
6a	2,3-M/(2*R*)-*cis*	5.4 ± 1.1	18	57	113 ± 30	24	−1.4	0.048
***ent*-6a**	2,3-M/(2*S*)-*cis*	172 ± 39	5.0	41	222 ± 23	47	6.4	0.77
5b	2,3-M/(2*S*)-*trans*	4.4 ± 0.2	0	99	5.5 ± 0.6	0	100	0.80
***ent*-5b**	2,3-M/(2*R*)-*trans*	21.1 ± 5.1	0	99	23.2 ± 3.6	5.0	94	0.91
6b	2,3-M/(2*R*)-*cis*	110 ± 16	1.8	90	172 ± 40	3.2	72	0.64
***ent*-6b**	2,3-M/(2*S*)-*cis*	103 ± 13	6.7	86	33.5 ± 2.9	15	68	3.1
AEIC (**3**)[e]	1,2-M[d]/(1*S*)-*cis*	1.3 ± 0.2	100	—	—	—	—	—
(*R*)-CEIC (**4**)[f]	1,2-M/(1*R*)-*trans*	8.4 ± 1.5	0	100	7.6 ± 0.4	0	>100	1.1
(*S*)-CEIC (***ent*-4**)[f]	1,2-M/(1*S*)-*trans*	3.6 ±0.4	0	100	37.2 ±2.7	0	>100	0.097
Thioperamide[f]	—	51.1 ± 3.8	—	99	124 ±14	—	90	0.41

[a] Assay was carried out with cell membranes expressing human H_3 or H_4 receptor subtypes (n = 3–4). [b] Relative potency of compound (10^{-5} M) to histamine (10^{-5} M) for the receptor activation. [c] Inhibitory effect of compound (10^{-5} M) on the agonistic activity of histamine (10^{-6} M). [d] 1,2-M and 2,3-M mean 1,2-methano and 2,3-methano, respectively. [e] Data with rat H_3 receptor taken from ref. 6b. [f] Data taken from ref. 6c.

remarkably more potent activity (K_i < 30 nM) than the well-known H_3 receptor antagonist thioperamide (K_i = 51.1 nM). On the other hand, the *cis*-analogs showed relatively weaker affinity for the H_3 receptor than the *trans*-analogs, except for the (2*R*)-*cis*-analog **6a** (K_i = 5.4 nM). In order of the binding affinities, these compounds ranked as **5b**, **6a** > ***ent*-5a** > **5a**, ***ent*-5b** > ***ent*-6b**, **6b** > ***ent*-6a**, where ***ent*-5a**, **6a**, and **5b** had a significant nM level K_i.

The binding affinities of the compounds for the human H_4 receptor subtype are also summarized in Table 1. The *trans*-analogs, **5b**, ***ent*-5b**, and *cis*-analog ***ent*-6b** had significant activity ($K_i \leq 30$ nM), with **5b** being the most potent (K_i = 5.5 nM).

The relative affinity of these compounds for the H_3 and the H_4 receptors would indicate that a hydrophobic group might be required for high affinity for the H_4 receptor but not for the H_3 receptor, as shown with the non-hydrophobic analog **6a** (K_i = 5.4 nM for H_3, K_i = 113 nM for H_4) and the hydrophobic analog **5b** (K_i = 4.4 nM for H_3, K_i = 5.5 nM for H_4). Our results are consistent with the previous reports on the histamine receptor ligands.[11]

The function of the compounds on human histamine H_3 and H_4 receptor subtypes, which were expressed individually in 293-EBNA cells, was next investigated by luciferase reporter gene assay.[6b] The results are also summarized in Table 1.

All the **b**-series compounds having a hydrophobic 4-chlorobenzyl function were antagonists in accordance with the previous results of the histamine receptor ligands.[2b,6c] The (2*S*)-*trans*-analog **5b** with the 2,3-methanobutane backbone was a highly potent antagonist to both the H_3 and H_4 receptors with K_i values of 4.4 nM (for H_3) and 5.5 nM (for H_4), which was more potent than its regioisomeric parent compound (*R*)-CEIC (**4**) with the 1,2-methanobutane backbone. While (*S*)-CEIC (***ent*-4**) with the 1,2-methanobutane backbone was a H_3 receptor selective antagonist (K_i (H_3)/K_i (H_4) = 0.097), its regioisomeric *trans*-analog ***ent*-5b** with the 2,3-methanobutane backbone showed non-selective moderate antagonistic effects on both of the receptors (K_i (H_3)/K_i (H_4) = 0.91).

Based on the previous SAR studies on H_3 and H_4 receptor ligands,[2a,6b] we expected that the **a**-series compounds having the primary amino side-chain without a hydrophobic group would be full agonists. However, the activation potencies for the receptors of these compounds relative to histamine were less than 50%, as shown in Table 1. These results indicate that ***ent*-5a**, **6a**, and ***ent*-6a** work as partial agonists to both of the H_3 and H_4 receptors. Furthermore, compound **5a** with the (2*S*)-*trans*-cyclopropane structure almost completely inhibited activation of the H_3 receptor by histamine (94% inhibition). Thus, although **5a** does not have a hydrophobic group which H_3 receptor antagonists usually have, unexpectedly, it was shown to be an H_3 receptor antagonist.[12] Compound **6a** is the regioisomeric *cis*-2,3-methanobutane analog of the parent compound AEIC (**3**) with the *cis*-1,2-methanobutane backbone, and both **6a** and **3** are selectively and highly active at the H_3 receptor (K_i = 5.4 nM and 1.3 nM, respectively). However, these two regioisomers have functionally different effects on the receptor, *i.e.*, **6a** was a partial agonist (18% activation), while **3** was a full agonist (100% activation).

Docking simulation by homology modeling

We previously constructed a three-dimensional model of the H_3 receptor[6d] based on a structural template from the crystal structure of the human β_2-adrenergic GPCR recently reported by Cherezov and co-workers.[5a] Using the model, docking simulations of a series of cyclopropane-based H_3 receptor ligands were performed and a reliable correlation between binding score and pK_i was obtained.[6d]

Therefore, in order to investigate the binding modes of the conformationally restricted analogs with the 2,3-methanobutane backbone to the H_3 receptor, docking simulations of the three potent ligands (***ent*-5a**, **6a**, and **5b**) and also the three less potent ligands (***ent*-6a**, **6b**, and ***ent*-6b**) were carried out by using the H_3 receptor homology model described above, and the binding modes were compared with that of AEIC (**3**) with the 1,2-methanobutane backbone. As shown in Fig. 4a, the proposed binding modes of the three potent ligands are well-superimposed with that of the potent lead compound **3**, especially at the imidazole ring and the basic nitrogen, which are important for the binding to the receptor. On the other hand, as shown in Fig. 4b, the proposed binding modes of the three less potent ligands and that of **3** are not as well superimposed. These results suggest that this homology

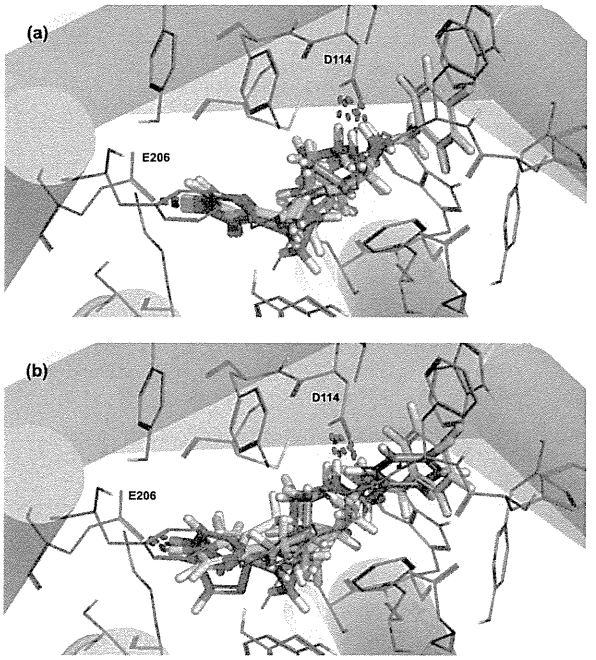

Fig. 4 Proposed models for the three potent ligands ***ent*-5a**, **6a**, **5b** and the lead compound **3** (a) and the three less potent ligands **6b**, ***ent*-6a**, ***ent*-6b** and **3** (b) binding to the homology model of the H_3 receptor[6d] from docking simulation. Carbon atoms are shown in magenta for **3**, cyan for **5b** and **6b**, yellow for **6a** and ***ent*-6a**, and orange for ***ent*-5a** and ***ent*-6b**, respectively. Hydrogen bonding and salt bridge between side-chain carboxyl group of Glu206 and an imidazole of the ligands, and between that of Asp114 and an amino group of the ligands are depicted by red dots.

model can be useful for investigation the binding modes of the H_3 receptor ligands and that the bioactive conformations of these potent ligands are analogous.

As described above, the stereochemical diversity-oriented conformational restriction strategy, employing the 2,3-methanobutane backbone, was shown to be useful for developing potent ligands of the H_3 and/or H_4 receptor in this study. It is important to note that, in addition to the previously used 1,2-methanobutane backbone, the regioisomeric 2,3-methanobutane backbone also worked effectively as an alternative cyclopropane-based conformational restriction structure. Thus, the combinational use of these two backbones not only increases the stereochemical diversity but also increases three-dimensional structural diversity of the compounds in this strategy, which can provide a variety of active compounds with different pharmacological properties.

Conclusions

We designed a series of conformationally restricted histamine analogs with a chiral *trans*- or *cis*-2,3-methanobutane backbone based on the stereochemical diversity-oriented strategy. These four stereochemical types of analogs were systematically synthesized from optically active epichlorohydrins *via* the versatile chiral cyclopropane units. Pharmacological properties of these analogs for the human H_3 and H_4 receptors were shown to be different depending on the stereochemistry of the cyclopropane backbones. Among the hydrophobic analogs (**b**-series), a *trans*-cyclopropane structure was preferred to a *cis*-cyclopropane one for both the H_3 and H_4 receptors. On the other hand, among the non-hydrophobic analogs (**a**-series), the structure of the most potent analog **6a** to both of the receptor subtypes was a *cis*-cyclopropane. In this study, a couple of potent H_3 and/or H_4 receptor ligands with a low nM K_i were identified. Analog **6a**, which has a (2*R*)-*cis*-2,3-methanobutane backbone, was the highest selective H_3 ligand, and analog **5b**, which has a (2*S*)-*trans*-2,3-methanobutane backbone, was the most potent H_3/H_4 dual ligand. Thus, the 2,3-methanobutane backbone worked effectively as the backbone of the conformationally restricted histamine analogs with stereochemical diversity as well as the 1,2-methanobutane. These differences in the stereochemistry of these backbones affected the potency and selectivity of the ligands. Therefore, the stereochemical diversity-oriented approach can be an effective strategy in medicinal chemistry studies.

Experimental

Chemical shifts (δ) are reported in ppm downfield from Me_4Si or CD_2HOD (3.31 ppm) (^1H) and $CDCl_3$ (77.0 ppm) or CD_3OD (49.0 ppm) (^{13}C). All of the ^1H-NMR assignments described were in agreement with COSY spectra. Thin-layer chromatography was done on Merck coated plate $60F_{254}$. Silica gel, Iatron beads and NH silica gel chromatographies were done on Merck silica gel 5715, Iatron 6RS-8060 (Mitsubishi Kagaku Iatron, Inc), and Chromatorex® (Fuji Silysia Chemical Ltd.), respectively. Reactions were carried out under an argon atmosphere except for hydrous reactions.

(2*S*,3*R*)-4-*tert*-Butyldiphenylsilyloxy-2,3-methanobutyraldehyde (7)

To a suspension of $MeOCH_2PPh_3Cl$ (3.63 g, 10.6 mmol) in THF (50 mL) was added $NaN(TMS)_2$ (1.0 M in THF, 9.12 mL, 9.12 mmol) at 0 °C, and the mixture was stirred at the same temperature for 20 min. To the resulting solution was added a solution of **1**[6a] (2.27 g, 7.60 mmol) in THF (10 mL) at 0 °C, and the reaction mixture was stirred at the same temperature for 5 h. After addition of saturated aqueous NH_4Cl, the solvent was evaporated, and the residue was partitioned between AcOEt and saturated aqueous NH_4Cl. The organic layer was washed with brine, dried (Na_2SO_4) and evaporated. The residue was purified by silica gel column chromatography (3% AcOEt in hexane) to give the enol ether product as an oil. To a solution of the product in acetone (40 mL) was added aqueous HCl (12 M, 20 mL), and the mixture was vigorously stirred at 0 °C for 10 s. Immediately, the mixture was poured into saturated aqueous $NaHCO_3$ (300 mL), and the resulting solution was extracted with AcOEt. The organic layer was washed with saturated aqueous $NaHCO_3$, brine, dried (Na_2SO_4) and evaporated. The residue was purified by silica gel column chromatography (5% AcOEt in hexane) to give **7** (2.27 g, 85%) as a colorless oil: $[\alpha]_D^{22}$ −12.0 (*c* 0.95, $CHCl_3$); ^1H-NMR (400 MHz, $CDCl_3$) δ 0.35 (1 H, m, cyclopropyl-CH_2), 0.52 (1 H, m, cyclopropyl-CH_2), 0.84 (1 H, m, cyclopropyl-CH), 0.91 (1 H, m, cyclopropyl-CH), 1.01 (9 H, s, *t*Bu), 2.27 (2 H, m, CH_2CHO), 3.49

(1 H, dd, J = 6.4, 10.7 Hz, CH_2OTBDPS), 3.69 (1 H, dd, J = 5.7, 10.7 Hz, CH_2OTBDPS), 7.35–7.44 (6 H, m, aromatic), 7.51–7.72 (4 H, m, aromatic), 9.75 (1 H, dd, J = 2.1, 2.3 Hz, CHO); ^{13}C-NMR (100 MHz, $CDCl_3$) δ 9.5, 10.2, 19.4, 20.5, 27.0, 47.6, 66.6, 127.5, 129.5, 133.7, 135.4, 201.9; LRMS (FAB) m/z 353 [(M+H)$^+$]; HRMS (FAB) calcd for $C_{22}H_{29}O_2Si$ 353.1937, found 353.1928 [(M+H)$^+$]; Found: C, 75.13; H, 8.05. Calc. for $C_{22}H_{28}O_2Si$: C, 74.95; H, 8.01%.

(2*R*,3*S*)-4-*tert*-Butyldiphenylsilyloxy-2,3-methanobutyraldehyde (*ent*-7)

Compound ***ent*-7** (2.41 g, 83%, colorless oil) was prepared from ***ent*-1**[6a] (2.80 g, 8.27 mmol) as described for the preparation of **7**: $[\alpha]_D^{22}$ +11.5 (c 0.98, $CHCl_3$); LRMS (FAB) m/z 353 [(M+H)$^+$]; HRMS (FAB) calcd for $C_{22}H_{29}O_2Si$ 353.1937, found 353.1925 [(M+H)$^+$]; Found: C, 75.02; H, 7.98. Calc. for $C_{22}H_{28}O_2Si$: C, 74.95; H, 8.01%. ^{1}H- and ^{13}C-NMR spectra were consistent with those of **7**.

(2*R*,3*R*)-4-*tert*-Butyldiphenylsilyloxy-2,3-methanobutyraldehyde (10)

Compound **10** (2.27 g, 92%, colorless oil) was prepared from **2**[6c] (2.37 g, 7.00 mmol) as described for the preparation of **7**: $[\alpha]_D^{24}$ −0.8 (c 1.15, $CHCl_3$); ^{1}H-NMR (400 MHz, $CDCl_3$) δ 0.05 (1 H, dd, J = 5.4, 10.6 Hz, cyclopropyl-CH_2), 0.77 (1 H, m, cyclopropyl-CH_2), 1.04 (9 H, s, tBu), 1.08–1.26 (2 H, m, cyclopropyl-CH ×2), 2.32 (1 H, m, CH_2CHO), 2.51 (1 H, m, CH_2CHO), 3.43 (1 H, dd, J = 8.8, 11.3 Hz, CH_2OTBDPS), 3.89 (1 H, dd, J = 5.4, 11.3 Hz, CH_2OTBDPS), 7.35–7.43 (6 H, m, aromatic), 7.64–7.69 (4 H, m, aromatic), 9.83 (1 H, t, J = 1.8 Hz, CHO); ^{13}C-NMR (100 MHz, $CDCl_3$) δ 8.79, 9.30, 17.1, 19.2, 26.9, 42.9, 63.8, 127.6, 129.6, 133.6, 135.4, 135.5, 202.3; LRMS (FAB) m/z 353 [(M+H)$^+$]; HRMS (FAB) calcd for $C_{22}H_{29}O_2Si$ 353.1937, found 353.1938 [(M+H)$^+$]; Found: C, 74.90; H, 8.01. Calc. for $C_{22}H_{28}O_2Si$: C, 74.95; H, 8.01%.

(2*S*,3*S*)-4-*tert*-Butyldiphenylsilyloxy-2,3-methanobutyraldehyde (*ent*-10)

Compound ***ent*-10** (2.15 g, 80%, colorless oil) was prepared from ***ent*-2**[6c] (2.62 g, 7.68 mmol) as described for the preparation of **7**: $[\alpha]_D^{24}$ +0.14 (c 1.02, $CHCl_3$); LRMS (FAB) m/z 353 [(M+H)$^+$]; HRMS (FAB) calcd for $C_{22}H_{29}O_2Si$ 353.1937, found 353.1940 [(M+H)$^+$]; Found: C, 75.07; H, 8.11. Calc. for $C_{22}H_{28}O_2Si$: C, 74.95; H, 8.01%. ^{1}H- and ^{13}C-NMR spectra were consistent with those of **10**.

(2*S*,3*R*)-4-*tert*-Butyldiphenylsilyloxy-2,3-methano-1-(1-triphenylmethyl-1*H*-imidazol-4-yl)butane (8)

To a suspension of tosylmethyl isocyanide (667 mg, 3.43 mmol) and **7** (1.21 g, 3.43 mmol) in absolute EtOH (8 mL) was added sodium cyanide (17 mg, 0.34 mmol) at 0 °C, and the resulting mixture was stirred at the same temperature for 30 min. After the solvent was evaporated, the residue in a saturated solution of ammonia in absolute EtOH (60 mL) was heated at 120 °C in a steel tube for 24 h. After cooling, the solvent was evaporated, and the residue was co-evaporated with pyridine (×3). After drying the residue *in vacuo*, a solution of the residue and trityl chloride (954 mg, 3.43 mmol) in pyridine (10 mL) was stirred at room temperature for 12 h. After the solvent was evaporated, the residue was partitioned between AcOEt and aqueous HCl (1 M). The organic layer was washed with saturated aqueous $NaHCO_3$, brine, dried (Na_2SO_4), and evaporated. The residue was purified by silica gel column chromatography (20–50% AcOEt in hexane) to give **8** (1.03 g, 48%) as a colorless oil: $[\alpha]_D^{22}$ −18.7 (c 1.10, $CHCl_3$); ^{1}H-NMR (400 MHz, $CDCl_3$) δ 0.31–0.39 (2 H, m, cyclopropyl-CH_2), 0.81–0.90 (2 H, m, cyclopropyl-CH ×2), 1.02 (9 H, s, tBu), 2.41 (1 H, dd, J = 6.8, 15.9 Hz, CH_2-imidazole), 2.59 (1 H, dd, J = 5.9, 15.9 Hz, CH_2-imidazole), 3.40 (1 H, dd, J = 6.3, 10.9 Hz, CH_2OTBDPS), 3.60 (1 H, dd, J = 5.4, 10.9 Hz, CH_2OTBDPS), 6.52 (1 H, s, imidazolyl) 7.11–7.13 (6 H, m, aromatic), 7.25–7.39 (16 H, m, aromatic & imidazolyl), 7.64–7.65 (4 H, m, aromatic); ^{13}C-NMR (100 MHz, $CDCl_3$) δ 9.86, 15.8, 19.2, 20.4, 26.8, 32.2, 67.0, 75.0, 117.8, 127.5, 127.9, 129.4, 129.7, 134.0, 135.6, 138.2, 141.4, 142.5; LRMS (FAB) m/z 633 [(M+H)$^+$]; HRMS (FAB) calcd for $C_{43}H_{45}N_2OSi$ 633.3301; found 633.3299 [(M+H)$^+$]; Found: C, 81.55; H, 7.05; N, 4.37. Calc. for $C_{43}H_{44}N_2OSi$: C, 81.60; H, 7.01; N, 4.43%.

(2*R*,3*S*)-4-*tert*-Butyldiphenylsilyloxy-2,3-methano-1-(1-triphenylmethyl-1*H*-imidazol-4-yl)butane (*ent*-8)

Compound ***ent*-8** (755 mg, 43%, colorless oil) was prepared from ***ent*-7** (970 mg, 2.75 mmol) as described for the preparation of **8**: $[\alpha]_D^{22}$ +18.3 (c 1.35, $CHCl_3$); LRMS (FAB) m/z 633 [(M+H)$^+$]; HRMS (FAB) calcd for $C_{43}H_{45}N_2OSi$ 633.3301; found 633.3300 [(M+H)$^+$]; Found: C, 81.38; H, 6.91; N, 4.60. Calc. for $C_{43}H_{44}N_2OSi$: C, 81.60; H, 7.01; N, 4.43%. ^{1}H- and ^{13}C-NMR spectra were consistent with those of **8**.

(2*R*,3*R*)-4-*tert*-Butyldiphenylsilyloxy-2,3-methano-1-(1-triphenylmethyl-1*H*-imidazol-4-yl)butane (11)

Compound **11** (744 mg, 51%, colorless oil) was prepared from **10** (821 mg, 2.33 mmol) as described for the preparation of **8**: $[\alpha]_D^{23}$ +4.9 (c 1.01, $CHCl_3$); ^{1}H-NMR (400 MHz, $CDCl_3$) δ 0.04 (1 H, m, cyclopropyl-CH_2), 0.66 (1 H, m, cyclopropyl-CH_2), 1.03 (9 H, s, tBu), 1.07–1.18 (2 H, m, cyclopropyl-CH ×2), 2.39 (1 H, dd, J = 7.9, 15.8 Hz, CH_2-imidazole), 2.75 (1 H, dd, J = 5.4, 15.8 Hz, CH_2-imidazole), 3.68 (2 H, d, J = 6.7 Hz, CH_2OTBDPS), 6.51 (1 H, s, imidazolyl) 7.11–7.13 (6 H, m, aromatic), 7.26–7.39 (16 H, m, aromatic & imidazolyl), 7.64–7.68 (4 H, m, aromatic); ^{13}C-NMR (100 MHz, $CDCl_3$) δ 10.0, 15.6, 18.2, 19.5, 27.2, 28.0, 64.5, 75.3, 118.0, 127.8, 127.9, 128.2, 128.2, 129.7, 130.1, 134.4, 134.4, 135.9, 135.9, 138.6, 142.3, 142.9; LRMS (FAB) m/z 633 [(M+H)$^+$]; HRMS (FAB) calcd for $C_{43}H_{45}N_2OSi$ 633.3301; found 633.3300 [(M+H)$^+$]. Found: C, 81.84; H, 6.81; N, 4.21. Calc. for $C_{43}H_{44}N_2OSi$: C, 81.60; H, 7.01; N, 4.43%.

(2*S*,3*S*)-4-*tert*-Butyldiphenylsilyloxy-2,3-methano-1-(1-triphenylmethyl-1*H*-imidazol-4-yl)butane (*ent*-11)

Compound ***ent*-11** (922 mg, 58%, a colorless oil) was prepared from ***ent*-10** (890 mg, 2.52 mmol) as described for the preparation of **8**: $[\alpha]_D^{23}$ −4.6 (c 0.96, $CHCl_3$); LRMS (FAB) m/z 633 [(M+H)$^+$]; HRMS (FAB) calcd for $C_{43}H_{45}N_2OSi$ 633.3301; found 633.3310 [(M+H)$^+$]; Found: C, 81.77; H, 6.89; N, 4.18. Calc. for